Math. Model. Nat. Phenom. 20 (2025) 3
https://doi.org/10.1051/mmnp/2024022

Mathematical Modelling of Natural Phenomena
www.mmnp-journal.org

MODELING FIBROUS DYSPLASIA PROGRESSION AND ITS THERAPEUTIC INTERVENTION

Juan C. Beltran-Vargas[1], Luis F. de Castro[2], Gabriel F. Calvo[1,*] and Víctor M. Pérez-García[1]

Abstract. Fibrous dysplasia (FD) is a rare, benign bone disorder characterized by the abnormal formation of tissue in a mosaic distribution. It can affect multiple bones, causing severe symptoms such as pathological fractures, spinal curvature, and reduced stature, as part of the so-called McCune–Albright Syndrome (MAS). FD originates from postzygotic gain-of-function mutations in the GNAS gene. While treatments for other skeletal diseases like the monoclonal antibody denosumab, used in osteoporosis, have been applied to FD, the absence of a quantitative understanding of the dynamics of lesional cell populations limits both in-depth analysis and therapy optimization. This study introduces a novel pharmacokinetic–pharmacodynamic mathematical model specifically designed for FD, enriched with *in vitro*/*ex vivo* data from denosumab assays. Our framework builds upon existing mathematical approaches for osteoporosis, focusing on two cell populations: (1) variant-bearing FD osteoprogenitors and (2) wild-type (WT) osteoprogenitors displaying transferred FD phenotypes. The resulting model paves the way for future *in vitro* assays targeting FD and related skeletal conditions. Our analyses reveal that abnormal cell proliferation in FD may be due to its atypical inhibition, providing new insights for potential treatment strategies. Furthermore, our simulations identify a promising biomarker for FD diagnosis.

Mathematics Subject Classification. 92D25, 37N25, 34K20, 35Q92, 34A34.

Received February 18, 2024. Accepted November 18, 2024.

1. Introduction

Fibrous dysplasia (FD) and McCune–Albright Syndrome (MAS) originate from a postzygotic gain-of-function mutation in the GNAS gene, specifically in the G stimulatory protein $G_s\alpha$. This genetic alteration drives the upregulation of cyclic adenylyl cyclase (cAMP) [1]. As a consequence, osteoprogenitors undergo altered differentiation, overproducing fibrous and undermineralized woven tissue, which results in fibro-osseous lesions [2]. These lesions manifest clinically as pain and deformities [3, 4]. Furthermore, involvement of GNAS mutations in certain endocrine organs induces their dysregulation [5], leading to conditions such as hyperthyroidism, precocious puberty, and elevated growth hormone production [6].

Keywords and phrases: Pharmacokinetic–pharmacodynamic mathematical modeling, fibrous dysplasia, McCune–Albright Syndrome, metabolic bone disease, osteoporosis, somatic mosaicism, RANKL/RANK/OPG signaling, vesicular RANK, denosumab.

[1] Department of Mathematics & Mathematical Oncology Laboratory (MOLAB), University of Castilla La-Mancha, Edificio Politecnico, Avda. Camilo Jose Cela s/n, Ciudad Real, 13071 Castilla La-Mancha, Spain.
[2] National Institutes of Health, Building 30, Room 209, MSC 4320, Bethesda, MD 20892-4320, USA.

* Corresponding author: gabriel.fernandez@uclm.es

Currently, there is no definitive cure for FD, with treatment strategies depending on the specific location and severity of the disease [7]. Many of these therapeutic approaches are adapted from those used in other skeletal disorders, such as osteoporosis [8]. One FDA-approved medication for FD is denosumab [9]. This antibody, initially developed for osteoporosis treatment in postmenopausal women and men at high risk of fractures [10], is also prescribed for other conditions of excessive osteoclastic activity, including metastatic bone cancer [11] and Paget's disease [12]. Its mechanism of action is the inhibition of osteoclastogenesis by binding to and neutralizing RANKL [13]—a type II membrane protein belonging to the tumor necrosis factor superfamily, which plays a crucial role in bone regeneration and remodeling. By doing so, denosumab reduces bone resorption, resulting in an overall increase in bone mineral density, and, consequently a decreased risk of fractures (see Fig. 1).

Several *in vitro*/*ex vivo* models have been established to replicate the physiopathology of FD [14–17], primarily by expressing the GNAS mutation within bone marrow stromal cells (BMSCs) under controlled conditions. *In vitro* models have revealed that while denosumab exerts no effect on BMSC proliferation, it strongly inhibits osteoclast activation, particularly through the RANKL/RANK/OPG pathway [18] in FD lesions. To date, while mathematical modeling has provided insights into bone resorption dynamics [19, 20], specifically in the context of osteoporosis and related interventions such as denosumab [21] and alendronate [22], a dedicated mathematical framework for FD remains elusive. It is noteworthy that GNAS mutations introduce substantial alterations to RANKL secretion mediated by the cAMP pathway [23, 24], thereby modulating bone resorption dynamics inherent to FD.

In this study, we introduce a novel PK/PD mathematical model tailored to FD and informed by *in vitro* assays with denosumab. It builds upon previous osteoporosis quantitative approaches based on ordinary differential equations, integrating recent pivotal findings [25, 26]. Our framework examines two key scenarios: (1) variant-bearing FD osteoprogenitor cells and (2) wild-type (WT) osteoprogenitor cells displaying transferred FD phenotypes [4]. Several sub-models are formulated to support various hypotheses. These address inhibition mechanisms affecting cell proliferation, the interplay between mutant and phenotype-transferred cells, the role of osteoclast degradation in FD, together with a number of relevant qualitative mathematical properties. Therefore, our model sets the stage for future *in vitro* assays targeting FD and other related skeletal disorders.

2. Derivation of the model

2.1. Fibrous dysplasia disorder

Bone remodeling is orchestrated by basic multicellular units comprising osteoblastic and osteoclastic cells. These cells are primarily responsible for bone formation and resorption, respectively [27]. The balanced interaction between these cell types is essential for maintaining healthy bone homeostasis. However, this balance is intricately influenced by complex signaling pathways and transcription factors, posing a challenge from a mathematical modeling viewpoint. An early modeling attempt by [19] focused on the RANKL/RANK/OPG pathway and the catabolic actions of the parathyroid hormone. This model was later refined in the context of osteoporosis to explore the PK/PD dynamics of denosumab [21]. Subsequent studies highlighted the importance of vesicular RANK [26] and the inhibitory effect of RANKL on mesenchymal stem cells [25] in osteoblastogenesis (see Fig. 1). While disorders such as osteoporosis and osteopetrosis are characterized by imbalances in bone resorption leading to net bone gain or loss, FD presents a unique difficulty. It originates from a postzygotic mutation in the GNAS gene, significantly disrupting bone homeostasis by altering osteoblastic differentiation [23] and amplifying osteoclastic activation *via* the RANKL/RANK/OPG pathway [18]. Moreover, FD tissue is composed not only by variant-bearing cells but also by WT cells that phenocopy the variant ones, mimicking the enhanced production of cAMP triggered by activating mutations in $G_s\alpha$ [4].

2.2. Model formulation

To illustrate the different elements of our model, we refer to Figure 2. WT tissue osteogenesis is conceptualized in three primary cellular compartments: (1) osteoprogenitors (P), (2) osteocytes (C_I), and (3) active osteoclasts (C_L). We consider stem cells as an external input and categorize osteoblasts into a transitional compartment

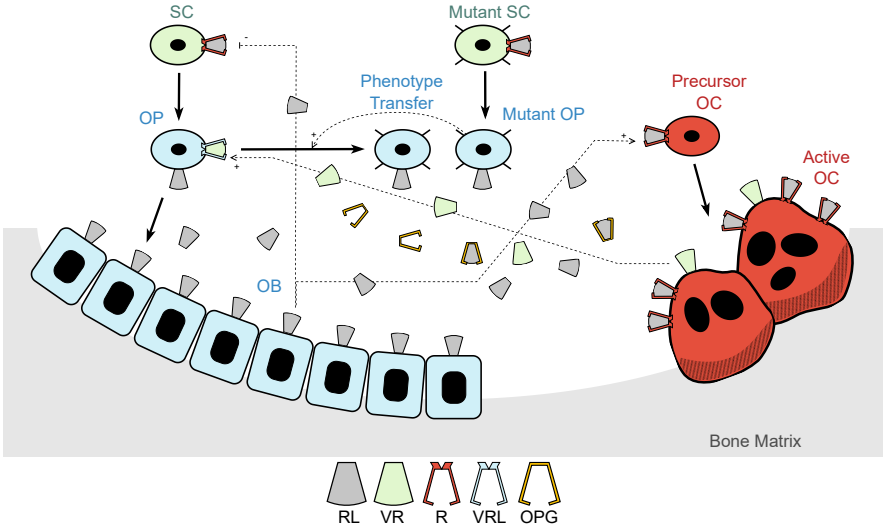

FIGURE 1. Schematic representation of key processes in fibrous displasia (adapted and extended from [21]). Vesicular RANK (VR) promotes the differentiation of WT osteoprogenitors (OP) into osteoblasts (OB), while RANKL (RL) inhibits stem cell (SC) differentiation and concurrently promotes osteoclast (OC) activation. Variant-bearing FD SCs differentiate into variant-bearing FD OPs, which exhibit impaired differentiation. Additionally, these mutant OPs can transfer their phenotype to WT OPs, thereby altering their behavior. Other abbreviations: RANK (R) and VR ligand (VRL).

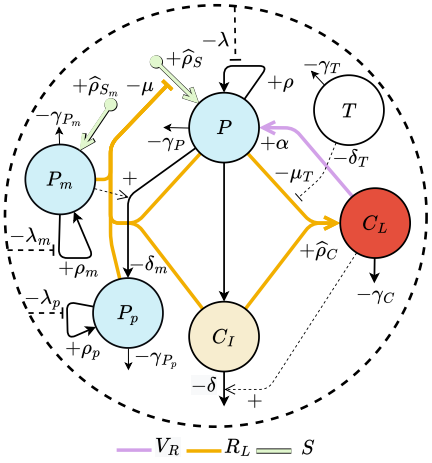

FIGURE 2. Schematic representation of the FD model. The finite size of the cell culture (dashed circumference) results in an inhibition ($-\lambda$) of proliferation ($+\rho$) and vesicular rank (V_R, in purple) promotes differentiation ($+\alpha$). RANKL (R_L, in yellow) is secreted by both osteoprogenitors (P) and osteocytes (C_I) and promotes osteoclast (C_L) activation ($+\hat{\rho}_C$). It also inhibits ($-\mu$) the incoming flow from the mesenchymal stem cells (S in green). Bone matrix is degraded ($-\delta$) by C_L, since it is proportional to C_I. Mutant osteoprogenitors (P_m) behave similarly to P, but with impaired differentiation. Additionally, P_m converts ($-\delta_m$) WT osteoprogenitors (P) into phenotype-transferred osteoprogenitors (P_p), which do not bear the mutation but mimic the behavior of P_m. Denosumab (T) binds (δ_T) to the RANKL protein, thereby limiting (μ_T) its effect on both stem cells and C_L.

that invariably differentiates into osteocytes. This model simplification deliberately excludes processes such as apoptosis and lining cell formation due to their limited relevance to the subsequent denosumab intervention. These compartments encapsulate the key elements for our analysis. After OPG inhibition, RANKL, denoted as effective RANKL (R_L), is produced by osteoprogenitors and osteocytes. Regarding the interplay between osteoclasts and osteocytes, osteoclast activation will be assumed to be strictly governed by the levels of effective RANKL in the cell culture medium, such that the osteoclast population increases with R_L. Conversely, since osteocytes are degraded by activated osteoclasts, the osteoclast population is inversely proportional to the osteocyte population, hence $C_L \propto R_L \propto C_I^{-1}$. Additionally, to incorporate FD tissue, two further compartments are introduced: (1) variant-bearing FD osteoprogenitors (P_m) and (2) WT osteoprogenitors exhibiting transferred FD phenotypes (P_p). These compartments share similar osteoprogenitor properties but display impaired differentiation.

We now include the role of the therapy (T), specifically denosumab, which is the FDA-approved antibody for FD. For mathematical convenience, unlike existing pharmacokinetic (PK) models [10, 28] for FD, we have simplified the PK component into a fully degenerative function that represents the antibody concentration in the cell culture plate. This concentration is inversely proportional to the effective RANKL and consequently to the osteoclast population, thus $T \propto R_L^{-1} \implies T \propto C_L^{-1}$. This simplification streamlines the model by assuming an instantaneous effect of denosumab, yet it does not affect the mid-term and long-term analyses. Consequently, the defined compartments are WT osteoprogenitors ($P(t)$), FD mutant cells ($P_m(t)$), FD phenotype-transferred cells ($P_p(t)$), osteocytes ($C_I(t)$), osteoclasts ($C_L(t)$), and the denosumab intervention ($T(t)$). Variables such as protein availability, mechanical pressure, cell type, and other factors can significantly influence the carrying capacity and its inhibitory effects in osteoprogenitor proliferation [29] and down-regulation of mesenchymal stem cells [25]. Considering logistic functions for modeling those inhibitory effects, including also those produced by the treatment pharmacodynamics (PD) component [9] over RANKL, the resulting system of autonomous ordinary differential equations (ODEs) reads as

$$\frac{\mathrm{d}P}{\mathrm{d}t} = \rho P(1-\lambda L)_+ + \hat{\rho}_S(1-\mu M)_+ - \alpha P - \delta_m P P_m, \tag{2.1a}$$

$$\frac{\mathrm{d}P_m}{\mathrm{d}t} = \rho_m P_m(1-\lambda_m L)_+ + \hat{\rho}_{S_m}(1-\mu_m M)_+, \tag{2.1b}$$

$$\frac{\mathrm{d}P_p}{\mathrm{d}t} = \rho_p P_p(1-\lambda_p L)_+ + \delta_m P P_m, \tag{2.1c}$$

$$\frac{\mathrm{d}C_I}{\mathrm{d}t} = \alpha P - \delta C_I C_L, \tag{2.1d}$$

$$\frac{\mathrm{d}C_L}{\mathrm{d}t} = \hat{\rho}_C M - \gamma_C C_L, \tag{2.1e}$$

$$\frac{\mathrm{d}T}{\mathrm{d}t} = -\delta_T T N - \gamma_T T, \tag{2.1f}$$

with $N = P + P_m + P_p + C_I$, $M = N(1-\mu_T T)_+$, $L = P + P_m + P_p + C_I + C_L$ and ρ, ρ_m, ρ_p, λ, λ_m, λ_p, α, γ_P, γ_{P_m}, γ_{P_p}, $\hat{\rho}_S$, $\hat{\rho}_{S_m}$, μ, μ_m, δ, $\hat{\rho}_C$, γ_C, δ_m, δ_T, γ_T, μ_T are defined in Table 1 together with their ranges.

2.3. Remarks

For mathematical and biological convenience, the subsequent analysis assumes that all parameters are real and positive (see Tab. 1). Introducing negative values could lead to biological inconsistencies, such as reverse mitosis with a negative ρ or dedifferentiation with a negative α. Although mathematically feasible, initial conditions such as $P(0), P_m(0), P_p(0), C_I(0)$, or $C_L(0)$ exceeding the maximum net population of L (derived from λL), are biologically improbable as they could imply impairments in cell adhesion, producing unrealistic debris in the culture. Given that the prior definition considered only logistic inhibition functions, a detailed

TABLE 1. Parameter definitions for the model of equation (2.1). Ranges estimated from numerical simulations (see Sect. 3.7). Rate units: day^{-1}. Coefficient units: dimensionless.

	Description	Range
ρ, ρ_m, ρ_p	Baseline proliferation rates	$(\alpha, 24]$
λ	Proliferation inhibition coefficient	$(0, 1]$
λ_m	Mutant proliferation inhibition coefficient	$(0, \lambda)$
λ_p	Phenocopied proliferation inhibition coefficient	$(0, \lambda)$
α	WT differentiation rate	$(0, \rho)$
$\hat{\rho}_S$	Stem cells net flow rate	$(0, \rho)$
$\hat{\rho}_{S_m}$	Mutant stem cells net flow rate	$(0, \rho_m)$
μ	Stem cell inhibition coefficient	$(0, 1]$
μ_m	Mutant stem cell inhibition coefficient	$(0, 1]$
δ	Bone resorption rate	$(0, 1]$
$\hat{\rho}_C$	Osteoclast activation rates	$(0, 1]$
γ_C	Osteoclast deactivation rate	$(0, 1]$
δ_m	Mutant conversion rate	$(0, 1]$
δ_T	Treatment binding rate	$(0, 1]$
γ_T	Treatment degradation rate	$(0, 1]$
μ_T	Treatment's regulator coefficient	$(0, 1]$

mathematical model is presented in Appedix A, which also explores a Michaelis–Menten (MM) inhibition as an alternative. We have also examined several fundamental qualitative mathematical properties of the model (see Appendix B), including the positivity and boundedness of solutions. These analyses reinforce the model's validity and its applicability to realistic *in vitro* scenarios of FD. For additional results on the properties of WT and FD tissues, we refer the reader to Appendixes C and D, respectively.

3. Numerical simulations

3.1. Estimation of proliferation and inhibition parameters

To find these parameters from publicly accessible experimental datasets, we first consider the model in its simplest form, *i.e.* considering $\rho_m = \rho_p = \lambda_m = \lambda_p = \hat{\rho}_S = \hat{\rho}_{S_m} = \mu = \mu_m = \alpha = \delta_m = \gamma_{P_m} = \gamma_{P_p} = \delta = \hat{\rho}_C = \gamma_C = \mu_T = \delta_T = \gamma_T = P_m(0) = P_p(0) = C_I(0) = C_L(0) = T(0) = 0$ and $1 - \lambda P \geq 0$ in equation (2.1). In that way, we focus only on the proliferation and inhibition terms of WT osteoprogenitors without any stem cells contributions. Thus, the model (Eq. 2.1) becomes

$$\frac{\mathrm{d}P}{\mathrm{d}t} = \rho P(1 - \lambda P), \tag{3.1}$$

which describes the WT cell population growth. Analogously, by setting $\rho = \rho_p = \lambda = \lambda_p = \hat{\rho}_S = \hat{\rho}_{S_m} = \mu = \mu_m = \alpha = \delta_m = \delta = \hat{\rho}_C = \gamma_C = \mu_T = \delta_T = \gamma_T = P(0) = P_p(0) = C_I(0) = C_L(0) = T(0) = 0$ and $1 - \lambda_m P_m \geq 0$, we consider only the variant-bearing FD osteoprogenitors P_m without any stem cells contribution. Hence,

$$\frac{\mathrm{d}P_m}{\mathrm{d}t} = \rho_m P_m(1 - \lambda_m P_m), \tag{3.2}$$

describes the mutant cell population growth alone. According to the results obtained in [18] and summarized in Table 2, two sets of parameters, θ_1 and θ_2, defined as

$$\text{WT: } \theta_1 = \{\rho\}, \theta_2 = \{\rho, \lambda\}, \tag{3.3a}$$

$$\text{FD: } \theta_1 = \{\rho_m\}, \theta_2 = \{\rho_m, \lambda_m\}, \tag{3.3b}$$

TABLE 2. Normalized population doubling times (PDT) from BMSCs of healthy volunteers (HV) and FD patients [18]. $\hat{\mu}$: PDT sample mean. $\hat{\sigma}$: PDT sample standard deviation. IgG2: isotype Control Antibody. PDT at different days is expressed relative to cell number at day 0.

	HV				FD			
Day	IgG2		Denosumab		IgG2		Denosumab	
	$\hat{\mu}$	$\hat{\sigma}$	$\hat{\mu}$	$\hat{\sigma}$	$\hat{\mu}$	$\hat{\sigma}$	$\hat{\mu}$	$\hat{\sigma}$
0	1.00	0.00	1.00	0.00	1.00	0.00	1.00	0.00
2	1.46	0.72	1.70	0.11	1.67	0.43	1.85	0.46
9	4.43	0.34	4.25	0.67	10.92	2.65	15.35	1.13
16	8.72	2.65	6.87	0.87	22.53	4.53	29.33	7.20
23	9.51	1.85	13.35	3.98	36.61	6.20	36.64	3.00

TABLE 3. Results of the fitting of the proliferation and inhibition parameters for equations (3.1) and (3.2). Assuming that *in-vitro* cell growth follows a sigmoidal form, whose carrying capacity is denoted by λ in the logistic equation, then $\lambda = 9.51/9.51 = 1$ and $\lambda_m = 9.51/36.61 = 0.26$ are here considered to find only $\hat{\theta}_1$.

		WT		FD	
		value	CI	value	CI
$\hat{\theta}_1$	ρ	0.22	0.03	0	0
	ρ_m	–	–	0.28	0.07
$\hat{\theta}_2$	ρ	0.22	0.05	0	0
	ρ_m	–	–	0.28	0.09
	λ	0.92	0.40	0	0
	λ_m	–	–	0.26	0.12

are proposed for adjusting the models using the profile-likelihood method [30]. Here, we define the optimal estimator as $\hat{\theta}_j = \arg\min\left[\chi^2(\theta_j)\right]$, where $\chi^2(\theta_j) = \sum_{i=1}^{n}((\hat{\mu}_i - P(\theta_j, t_i))/\hat{\sigma}_i)^2$ is the likelihood function with mean $\hat{\mu}_i$, standard deviation $\hat{\sigma}_i$, n records and population $P(\theta_j, t_i)$ at time t_i with parameters θ_j. The likelihood-based confidence intervals (CI) are defined by $\{\theta_j | \chi^2(\theta_j) - \chi^2(\hat{\theta}_j) < \Delta_\alpha\}$ with $\Delta_\alpha = \chi^2(\alpha = 0.05, df = \#\theta_j)$. The results of calculating $\hat{\theta}_1$ and $\hat{\theta}_2$ are shown in Table 3 and represented in Figure 3. The uncertainty spaces around these estimators are also displayed in Figure 4. These regions reveal that both $\hat{\theta}_1$ and $\hat{\theta}_2$ are valid identifiable estimators.

Finally, considering $H_0 : \rho_m - \rho = 0$, the two sample t-statistic is calculated with $t = (\hat{\rho} - \hat{\rho}_m)/(\mathrm{CI}_\rho^2/5 + \mathrm{CI}_{\rho_m}^2/5)^{1/2}$, resulting in $t_{\hat{\theta}_1} = -1.762$ and $t_{\hat{\theta}_2} = -1.303$ for both estimators. Thus, the difference between the ρ terms is not statistically significant with $t(\alpha = 0.05, df = 4)$, since the p-value$_{\hat{\theta}_1} = P(|t_{\hat{\theta}_1}| \geq 1.762) = 0.1529$ and p-value$_{\hat{\theta}_2} = P(|t_{\hat{\theta}_2}| \geq 1.303) = 0.2625$. Similar result is likewise derived in the MM form presented in Appendix E. Therefore, the *in vitro* proliferation is governed by $\rho = \rho_m$, which implies $\lambda > \lambda_m$, suggesting that dysplastic cells are abnormally inhibited, instead of presenting an abnormal proliferation, such as $\rho_m \gg \rho$, which would not match current knowledge [6, 31, 32]. Notably, our findings challenge prevailing assumptions, providing substantial statistical evidence that the proliferation of FD may stem from compromised inhibitory mechanisms on cellular proliferation.

3.2. Stability and bifurcation analysis of FD and FD phenotype-transferred cells

To further explore the relationship between the WT and FD tissues, we will now focus on the interplay between P, P_m, and P_p, *i.e.*, taking $\hat{\rho}_S = \hat{\rho}_{S_m} = \mu = \mu_m = \alpha = \delta = \hat{\rho}_C = \gamma_C = \delta_T = \gamma_T = C_I(0) = C_L(0) = T(0) = 0$,

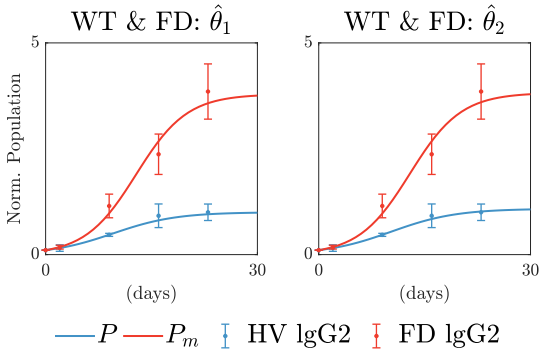

FIGURE 3. Proliferation curves for equations (3.1) and (3.2) with initial conditions $P(0) = 1/9.51$ and $P_m(0) = 1/9.51$, based on HV-IgG2 data from Table 3. The data were normalized by dividing each value by the maximum value of 9.51.

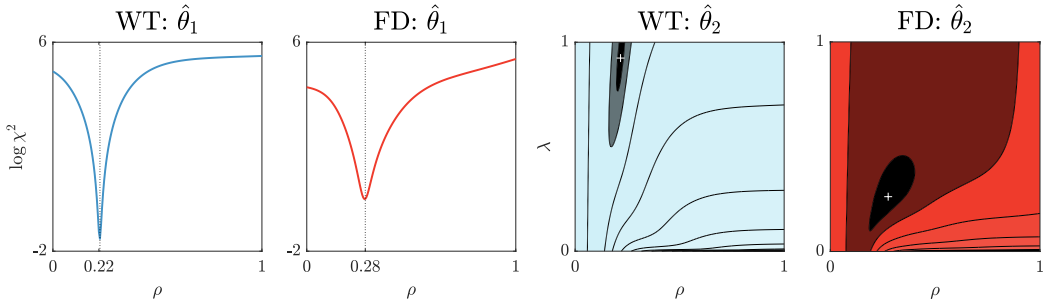

FIGURE 4. Likelihood surface for $\hat{\theta}_1$ and $\hat{\theta}_2$ in equations (3.1) and (3.2). Both estimators are identifiable.

$1 - \lambda L \geq 0$, $1 - \lambda_m L \geq 0$ and $1 - \lambda_p L \geq 0$ in model equation (2.1), leading to

$$\frac{\mathrm{d}P}{\mathrm{d}t} = \rho P(1 - \lambda(P + P_m + P_p)) - \delta_m P P_m, \tag{3.4a}$$

$$\frac{\mathrm{d}P_m}{\mathrm{d}t} = \rho_m P_m(1 - \lambda_m(P + P_m + P_p)), \tag{3.4b}$$

$$\frac{\mathrm{d}P_p}{\mathrm{d}t} = \rho_p P_p(1 - \lambda_p(P + P_m + P_p)) + \delta_m P P_m. \tag{3.4c}$$

Appendix F presents the steady states and Figure 5 shows the numerical stability and bifurcation with $\delta_m \in [0, 50]$ and $P(0)/P_m(0) \in [0, 2]$. Having established that FD excerts an abnormal inhibition, such that, $\lambda > \lambda_m$ and $\rho = \rho_m$, and considering that phenocopied cells present same abnormal inhibition than mutant cells, such that, $\lambda_m = \lambda_p$ and $\rho_m = \rho_p$, then equation (F.4) describes the stability of P and $P_m + P_p$. Consequently, denoting by P^*, P_m^* and P_p^* the steady states for equation (3.4), respectively, the simulations reveal that P_m^* and P_p^* depend of δ_m and the initial conditions $P(0)$, $P_m(0)$ and $P_p(0)$. Furthermore, the stability of P around $P^* = 0$ remains unaltered, irrespective to δ_m or the initial conditions. From a biological perspective, regardless of the presence of phenocopied cells, the preceding result indicates that FD cells decrease the WT cell population through resource competition by $\lambda > \lambda_m$.

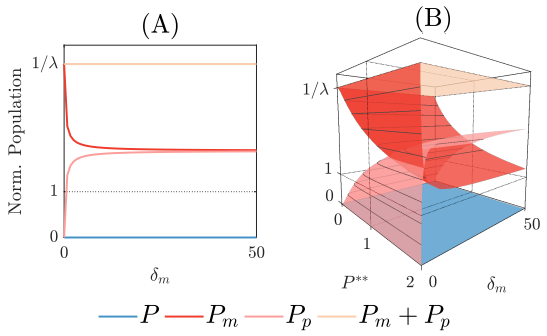

FIGURE 5. Bifurcation analysis for P and $P_m + P_p$ varying δ_m in equation (3.4) based on $\hat{\theta}_1$ from Table 3. (A) Bifurcation map illustrating also P_m and P_p with $P(0) = P_m(0)$ and $P_p(0) = 0$. (B) A 3D representation of the stability of P_m and P_p varying δ_m and $P^{**} \equiv P(0)/P_m(0)$. Long-term cell competition is described in equation (F.4). P_p is marginal to the stability of the healthy tissue. FD decrease WT cells by $\lambda > \lambda_m$.

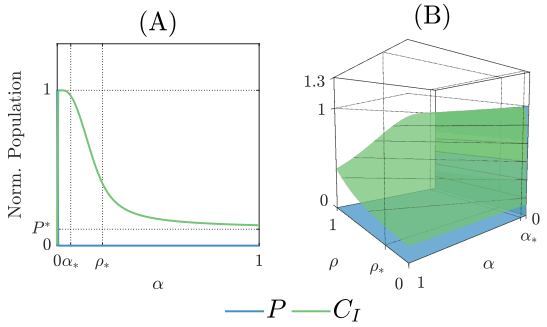

FIGURE 6. Bifurcation maps of WT osteoprogenitor's differentiation in equation (3.5). (A) Bifurcation in α with $\hat{\theta}_1$ from Table 3. (B) Bifurcation in ρ and α. ρ_*: ρ in $\hat{\theta}_1$. α_*: 1/16. The net population decreases substantially when α is close to ρ.

3.3. Upper bound for the differentiation rate

Considering that FD tissue exhibits an impairment in differentiation, the alternative for adjusting α relies on data from WT tissue. However, given the considerable variability of cell differentiation across experiments, establishing a similar analysis as before would be impractical. Hence, we will identify a subspace of valid solutions for α that holds significance from a biological perspective. Consequently, regarding only the osteoblastic lineage from the equivalent WT tissue model (see Eq. C.2 in Appendix C), we get

$$\frac{\mathrm{d}P}{\mathrm{d}t} = \rho P(1 - \lambda(P + C_I)) - \alpha P, \tag{3.5a}$$

$$\frac{\mathrm{d}C_I}{\mathrm{d}t} = \alpha P. \tag{3.5b}$$

The steady states are described in Appendix G. Figure 6 shows the bifurcation analysis with $\rho \in [0, 1]$ and $\alpha \in [0, 1]$, illustrating how the steady state of C_I tends to $P(0)$ when the differentiation rate increases. In particular, the net population experiences a significant decline when α increases. It is reasonable to consider

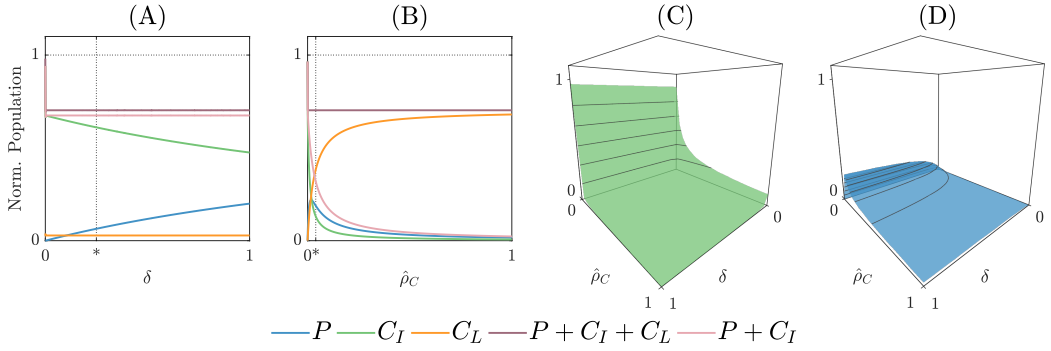

FIGURE 7. Osteoclastogenesis bifurcation for equation (3.7) varying δ and $\hat{\rho}_C$, with $\hat{\theta}_1$ from Table 3 and $\alpha = 1/16$, $\gamma_C = 1/30$. (A) Bifurcation varying δ_m. (B) Bifurcation varying $\hat{\rho}_C$. (C) Osteocyte's bifurcation surface. (D) Osteoprogenitor's bifurcation surface. * are the values used in later simulations: $\delta = 1/4$, $\hat{\rho}_C = 0.0014$. Variations in $\hat{\rho}_C$ reveal a stronger influence over bone matrix than variations in δ.

that differentiation is bounded by proliferation, such that,

$$\alpha \ll \rho. \tag{3.6}$$

Particularly, given that the carrying capacity is reached when no differentiation exists, then, for an experiment having a differentiation close to or larger than the proliferation rate, the net population will be substantially reduced. This result establishes initial boundaries for the stability conditions described in Appendix C.6.

3.4. Stability and bifurcation analysis of osteoclast cells

Upon the introduction of active osteoclasts in experimental settings, the bone resorption process is initiated. Although the dynamics of resorption may vary depending on the experimental design, it is crucial to elucidate the roles of factors like δ, $\hat{\rho}_C$ and γ_C in maintaining homeostasis. This understanding is necessary to capture the influence of the RANK/RANKL/OPG signaling pathway within the WT system, implicitly represented by the factors associated with M. Thus, considering the WT tissue model of (see Eq. C.2 in Appendix C) without the stem cells flow, results in

$$\frac{\mathrm{d}P}{\mathrm{d}t} = \rho P(1 - \lambda(P + C_I + C_L)) - \alpha P, \tag{3.7a}$$

$$\frac{\mathrm{dC}_I}{\mathrm{d}t} = \alpha P - \delta C_I C_L, \tag{3.7b}$$

$$\frac{\mathrm{dC}_L}{\mathrm{d}t} = \hat{\rho}_C(P + C_I) - \gamma_C C_L. \tag{3.7c}$$

The dynamics of equation (3.7) are studied in Appendix H. The trivial steady state (H.1) is stable for $\rho < \alpha$ and the non-trivial steady state (H.2) is stable when the parameters satisfy the condition $\rho > \alpha$. Having a fixed value for γ_C and using $\hat{\rho}_C$ to summarize all factors involved in osteoclast activation, including those related to fusion and aggressiveness [33], the model fitting and analysis is simplified, but C_L should be considered as a nucleus-based population, *i.e.*, a larger C_L implies more fusion events [34], instead of more osteoclast cells. The bifurcation maps varying $\hat{\rho}_C$ and δ are shown in Figure 7, revealing the inverse relation between active

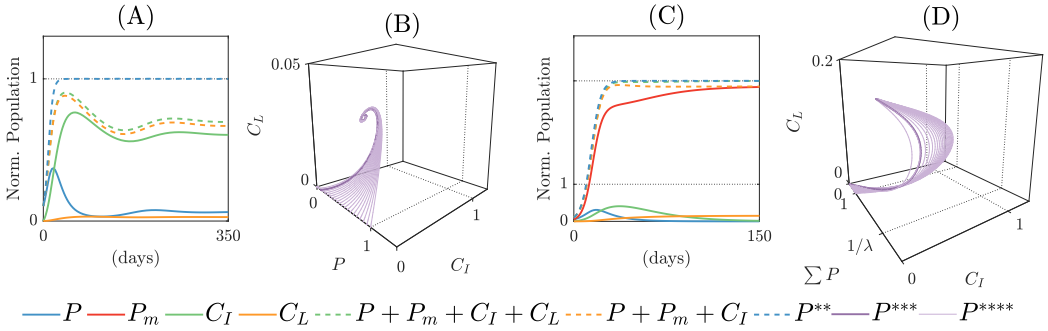

FIGURE 8. Phase maps for the WT tissue of equation (3.7) and the FD tissue of equation (3.8) without stem cells, with $\hat{\theta}_1$ from Table 3 and $\alpha = 1/16$, $\delta = 1/4$, $\hat{\rho}_C = 0.0014$, $\gamma_C = 1/30$. (A) Long-term simulation for WT tissue. (B) WT orbits. (C) Mid-term simulation for FD tissue. (D) FD orbits. P^{**} is the simulation curve of P from Figure 3. P^{***}: initial conditions $P(0) = P_m(0) = 1/9.51$ used in (A) and (C), respectively. P^{****}: additional simulations with initial conditions $P(0) = P_m(0) = [0, 1]$. In presence of mutant cells, the system stability changes from a spiral sink to an asymptotic sink.

osteoclasts and osteocytes described in (2.2), and a peak in the osteoprogenitor population when $\hat{\rho}_C$ is close to zero. This analysis also unveils a larger influence of $\hat{\rho}_C$ in the steady state of the osteocytes population than δ.

Notably, the model indicates that the collective activity of the osteoclast population exerts a greater influence on bone turnover than the intrinsic aggressiveness of individual osteoclasts. This suggests that reducing the overall osteoclast population is a more effective strategy for mitigating bone turnover. This finding aligns with the therapeutic approach of inhibiting the RANK/RANKL/OPG signaling pathway for the treatment of bone diseases.

3.5. Qualitative properties of stability between WT and FD cells

After characterizing resorption in WT tissue, it is crucial to further investigate the impact of mutant cells in bone resorption. Thus, appending just the mutant population P_m to the previous submodel (3.7), results in,

$$\frac{\mathrm{d}P}{\mathrm{d}t} = \rho P(1 - \lambda(P + P_m + C_I + C_L)) - \alpha P, \tag{3.8a}$$

$$\frac{\mathrm{d}P_m}{\mathrm{d}t} = \rho_m P_m(1 - \lambda_m(P + P_m + C_I + C_L)), \tag{3.8b}$$

$$\frac{\mathrm{dC}_I}{\mathrm{d}t} = \alpha P - \delta C_I C_L, \tag{3.8c}$$

$$\frac{\mathrm{dC}_L}{\mathrm{d}t} = \hat{\rho}_C(P + P_m + C_I) - \gamma_C C_L. \tag{3.8d}$$

This equation system is equivalent to the model of equation (2.1) with $\rho_p = \lambda_p = \hat{\rho}_S = \hat{\rho}_{S_m} = \mu = \mu_m = \delta_m = \gamma_{P_p} = \mu_T = \delta_T = \gamma_T = P_p(0) = T(0) = 0$, $1 - \lambda(P + P_m + C_I + C_L) \geq 0$ and $1 - \lambda_m(P + P_m + C_I + C_L) \geq 0$. The theoretical analysis is presented in Appendix I and the numerical simulations using $\hat{\theta}_1$ and $\alpha = 1/16$, $\delta = 1/4$, $\hat{\rho}_C = 0.0014$, $\gamma_C = 1/30$ are shown in Figure 8. These simulations elucidate how the stability deviates from a spiral sink in WT tissue (Eq. 3.7) to an asymptotic sink state in dysplastic tissue (Eq. 3.8). Features like shape, damping factor or eigenvalues of these stability states provide information that could assess the diagnosis of bone turnover disorders. Although, it is still possible to measure these features directly, it would

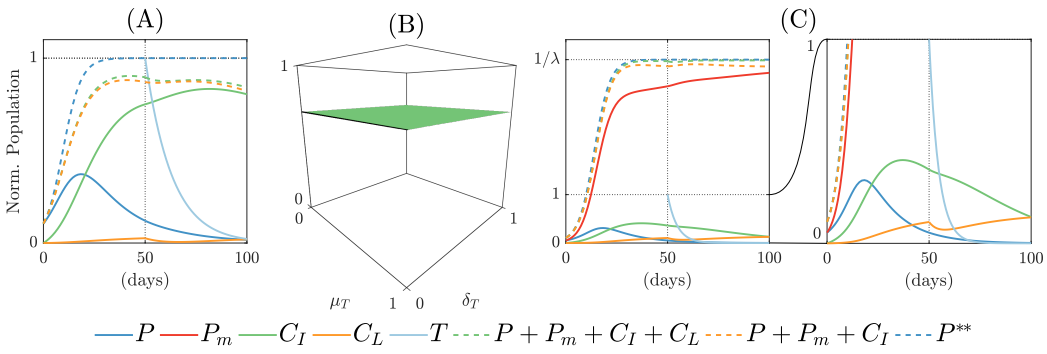

FIGURE 9. Denosumab intervention in $T(t=50)=1$ considering $\hat{\theta}_1$ from Table 3 and $\alpha = 1/16$, $\delta = 1/4$, $\hat{\rho}_C = 0.0014$, $\gamma_C = 1/30$. (A) WT treated tissue. (B) Treated osteocyte's bifurcation varying δ_T and μ_T. (C) FD treated tissue. P^{**} is the simulation curve of P from Figure 3. Steady states do not change after treatment, revealing just transitory effects.

be quite inefficient, since it would require cell counting for long periods of time. Therefore, this model suggests an efficient diagnosis biomarker for bone diseases on *in vitro* assays.

In clinical practice, patient assessment, medical history and imaging constitute the primary diagnostic modalities in FD [7]. However, many patients are asymptomatic and molecular analyses are still required [35], despite their limitations in accuracy [36]. Positively, the model offers preliminary indications of a novel diagnostic biomarker capable of enhancing diagnostic precision, based on the stability properties. The mutation in the GNAS gene alters the system's stability, facilitating the early detection of atypical cell populations by experimentally calibrating the model parameters. Thus, this approach has the potential to evolve into a novel diagnostic methodology for FD/MAS.

3.6. Study of the administration of denosumab

In order to investigate the therapeutic effects of denosumab within the proposed model system, the treatment compartment is integrated with the WT (Eq. 3.7) and FD tissues (Eq. 3.8). That is, considering equation (2.1) with $\rho_p = \lambda_p = \hat{\rho}_S = \hat{\rho}_{S_m} = \mu = \mu_m = \delta_m = \gamma_{P_p} = P_p(0) = 0$, then, no alteration in the system stability is revealed after denosumab intervention (see Appendix J), since $\mathrm{d}T/\mathrm{d}t$ is a fully degenerative function characterized by a stability state equal to 0, its effect on osteoclasts are nullified asymptotically, as depicted in Figure 9. Additionally, the variance sensitivity analysis (see Fig. 10) shows no relevant influence of μ_T, δ_T or γ_T.

These numerical simulations revealed that denosumab does not exert persistent effects on wild-type and fibrous tissues under resource limitations. Furthermore, the results indicate that long-term osteogenesis may be enhanced only through periodic reduction of osteoclast activation, applicable to both osteoporosis (WT model) and FD diseases. However, extended therapies present certain challenges upon denosumab withdrawal, such as the well-known rebound effect [10, 37]. In the context of FD, in agreement with Section 3.2, the limited effect on bone remodeling also stems from the impaired differentiation of mutant cells, which continue consuming resources and compete unfavorably against WT osteoblastic cells in the absence of a systemic antagonist that regulates their population. Consequently, treatments failing to counteract this competitive imbalance are likely to yield only transient effects.

3.7. Parameter synopsis

As mentioned earlier, available public data in FD is limited and not all published FD experiments provide their raw data, specially data related to protein concentration and cell populations over time. Therefore, some parameter boundaries have been established ad-hoc in order to address the simulations and theoretical analyses with biological consistency in concordance with the derived results (see Tab. 1). Essentially, proliferation should

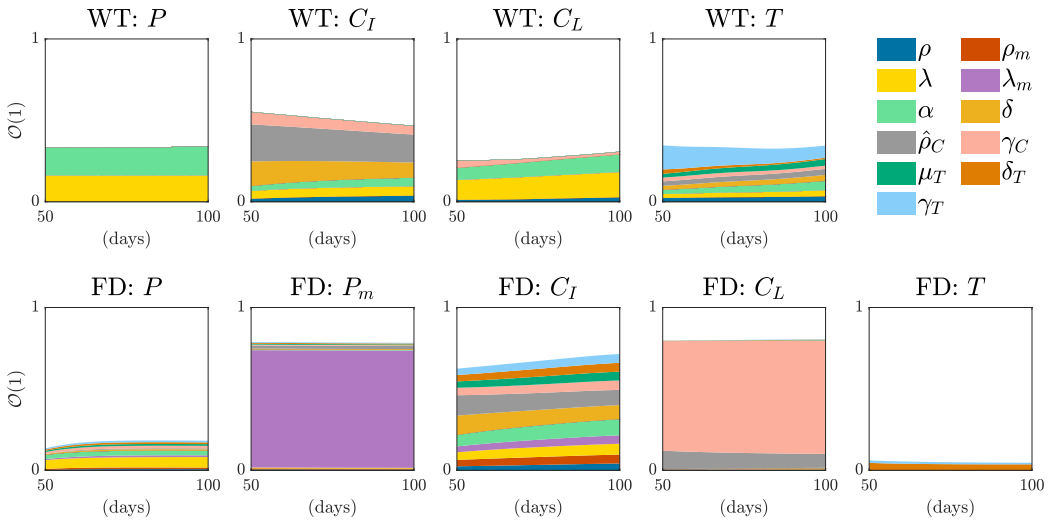

FIGURE 10. Stacked area chart with the variance sensitivity analysis for WT and dysplastic tissues after denosumab intervention in time $t = 50$. $P(0) = P_m(0) = 1/9.51$, $P_p(0) = C_I(0) = C_L(0) = T(0) = 0$ and $T(50) = 1$. First order Jansen–Sobol's indices [38] with $N \sim (1/2, 1/4)$ for all parameters and 1.5×10^6 iterations for $t = [50, 100]$. No relevant influence is found for μ_T, δ_T or γ_T.

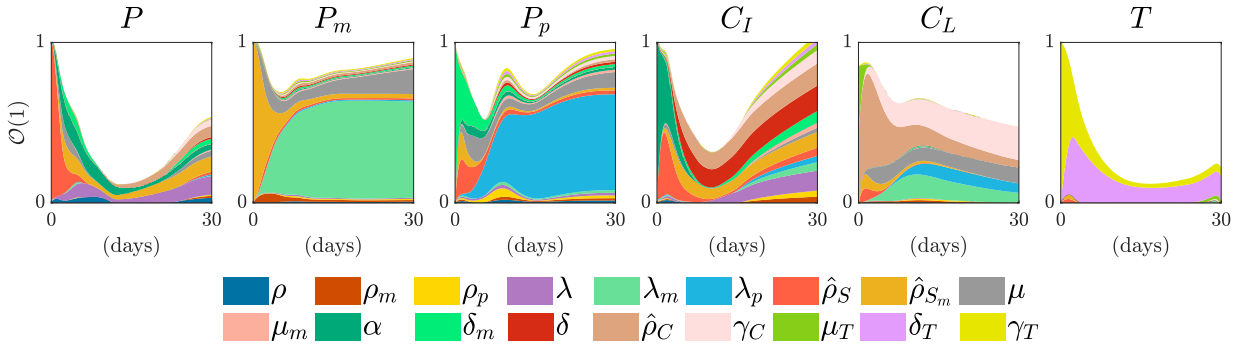

FIGURE 11. Stacked area chart with the variance-based sensitivity analysis with all parameters included for the first 30 days. $P(0) = P_m(0) = 1/9.51$, $P_p(0) = C_I(0) = C_L(0) = 0$ and $T(0) = 1$. Since the cell culture plate is almost empty in $t = 0$, the stem's flow, osteoclast activation and denosumab degradation are stronger in the first days. The mutant stem cells also have an indirect effect in the WT osteoprogenitors.

be larger than differentiation and lower than the minimum cell reproduction time, which should be around one hour, *i.e.*, 1/24 days. Alternatively, most parameters should be bounded from above by one day, although, they might not be consistent across all experimental trials due to differences in the design of each specific test run.

Finally, having these common boundaries, the first order Jansen–Sobol's indices [38] are computed for the model of equation 2.1 with $N \sim (1/2, 1/4)$ for all parameters and 1.5×10^6 iterations for the first 30 days and the results are shown in Figure 11.

4. Conclusions

In this study, we have proposed a comprehensive mathematical model designed to elucidate the intricate dynamics of fibrous dysplasia (FD) tissue response to denosumab treatment. Our model encapsulates bone resorption processes through the RANK/RANKL/OPG pathway, relevant to both wild-type (WT) and dysplastic bone tissues. It effectively integrates the key cellular populations involved in FD, aligning with existing empirical data from *in vitro* experiments. This innovative approach not only gives new insights into the fundamental mechanisms of FD progression but also demonstrates the potential implications for targeted therapeutic interventions.

Our findings challenge traditional views on FD progression, highlighting that this bone disorder may predominantly be driven by compromised inhibitory control on cell proliferation, rather than by direct stimulatory effects as previously thought. This result suggests that targeting those inhibitory pathways could be more effective than current standard strategies.

Moreover, based on the stability properties of the system modeled here, we have successfully identified potential ways to construct biomarkers for early FD diagnosis. These biomarkers would take into account the perturbations in equilibria produced by the mutation in the GNAS gene, which can be leveraged to identify FD cell populations early by adjusting the model parameters experimentally. This approach could enable earlier and more accurate detection of FD, significantly improving patient outcomes.

Cellular conditions may vary across *in vitro* assays, necessitating precise model fitting for each experiment. While fundamental differences between *in vitro* and *in vivo* assays limit direct model application beyond cell culture environments, the insights gained provide a foundational framework for further *in vitro* research. This aids in a deeper understanding of FD and potentially facilitates its extrapolation to *in vivo* contexts. Furthermore, this opens avenues for exploring optimal treatment strategies with denosumab or incorporating emerging therapies.

The versatility of the model extends beyond FD, offering a framework that could be adapted to study other bone diseases characterized by abnormal resorption processes, such as osteoporosis and osteopetrosis. This adaptability enhances the model's utility as a tool for broader biomedical research, potentially leading to breakthroughs in understanding and treating various bone disorders.

Additionally, from a more mathematical perspective, the model underscores the importance of selecting appropriate functional forms for inhibition modeling, advocating for logistic inhibition over Michaelis–Menten inhibition due to its simplicity and effectiveness in facilitating theoretical stability analysis. This approach simplifies the complex interactions within bone remodeling processes, making the model both accessible and applicable for further research and clinical application.

In conclusion, the contributions of this study are manifold, providing a detailed mathematical description of FD, proposing new diagnostic tools, and suggesting avenues for future research on bone pathology treatments. Our findings not only advance the understanding of FD but also set the stage for transformative impacts on the management and treatment of various bone-related diseases.

Acknowledgements

We gratefully acknowledge Magdalena Caballero (University of Córdoba) for proposing us the problem that led to this study and Juan Belmonte-Beitia (University of Castilla La-Mancha) for useful discussions. We also express our gratitude to Lina C. González-Cano, Jesús Cortés-Velasco and David G. Aragones (University of Castilla La-Mancha) for sharing their experience and ideas with us.

Funding

The work of VMPG and GFC has been partially supported by Ministerio de Ciencia e Innovación/Agencia Estatal de Investigación, Spain (doi:10.13039/501100011033, grant number PID2022-142341OB-I00) and European Regional Development Fund (ERDF A way of making Europe), by Junta de Comunidades de Castilla-La Mancha (grant number SBPLY/23/180225/000041), and by the University of Castilla-La Mancha, Applied Science Projects within the UCLM research programme (grant number 2022-GRIN-34405).

References

[1] L.S. Weinstein, A. Shenker, P.V. Gejman, M.J. Merino, E. Friedman and A.M. Spiegel, Activating mutations of the stimulatory g protein in the Mccune–Albright syndrome. *N. Engl. J. Med.* **325** (1991) 1688–1695. PMID: 1944469.

[2] J.Y. Wu, P. Aarnisalo, M. Bastepe, P. Sinha, K. Fulzele, M.K. Selig, M. Chen, I.J. Poulton, L.E. Purton, N.A. Sims, L.S. Weinstein and H.M. Kronenberg, Gαs enhances commitment of mesenchymal progenitors to the osteoblast lineage but restrains osteoblast differentiation in mice. *J. Clin. Invest.* **121** (2011) 3492–3504.

[3] M. Riminucci, B. Liu, A. Corsi, A. Shenker, A.M. Spiegel, P.G. Robey and P. Bianco, The histopathology of fibrous dysplasia of bone in patients with activating mutations of the $G\alpha_s$ gene: site-specific patterns and recurrent histological hallmarks. *J. Pathol.* **187** (1999) 249–258.

[4] S. Piersanti, C. Remoli, I. Saggio, A. Funari, S. Michienzi, B. Sacchetti, P.G. Robey, M. Riminucci and P. Bianco, Transfer, analysis, and reversion of the fibrous dysplasia cellular phenotype in human skeletal progenitors. *J. Bone Miner. Res.* **25** (2010) 1103–1116.

[5] P. Bianco, S.A. Kuznetsov, M. Riminucci, L.W. Fisher, A.M. Spiegel and P.G. Robey, Reproduction of human fibrous dysplasia of bone in immunocompromised mice by transplanted mosaics of normal and gsalpha-mutated skeletal progenitor cells. *J. Clin. Invest.* **101** (1998) 1737–1744.

[6] I. Hartley, M. Zhadina, M.T. Collins and A.M. Boyce, Fibrous dysplasia of bone and Mccune–Albright syndrome: a bench to bedside review. *Calcif. Tissue Int.* **104** (2019) 517–529.

[7] A.M. Boyce and M.T. Collins, Fibrous dysplasia/McCune–Albright syndrome: a rare, mosaic disease of $G\alpha_s$ activation. *Endocr. Rev.* **41** (2019) 345–370.

[8] I.R. Reid and E.O. Billington, Drug therapy for osteoporosis in older Adults. *Lancet* **399** (2022) 1080–1092.

[9] A.M. Boyce, W.H. Chong, J. Yao, R.I. Gafni, M.H. Kelly, C.E. Chamberlain, C. Bassim, N. Cherman, M. Ellsworth, J.Z. Kasa-Vubu, F.A. Farley, A.A. Molinolo, N. Bhattacharyya and M.T. Collins, Denosumab treatment for fibrous dysplasia. *J. Bone Miner. Res.* **27** (2012) 1462–1470.

[10] S. Ferrari and B. Langdahl, Mechanisms underlying the long-term and withdrawal effects of denosumab therapy on bone. *Nat. Rev. Rheumatol.* **19** (2023) 307–317.

[11] R.E. Coleman, P.I. Croucher, A.R. Padhani, P. Clézardin, E. Chow, M. Fallon, T. Guise, S. Colangeli, R. Capanna and L. Costa, Bone Metastases. *Nat. Rev. Dis. Primers* **6** (2020) 83.

[12] L. Corral Gudino, Paget's disease of bone: 1877–2023. Etiology, and management of a disease on epidemiologic transition. *Med. Clín. (Engl. Ed.)* **161** (2023) 207–216.

[13] D. Huang, C. Zhao, R. Li, B. Chen, Y. Zhang, Z. Sun, J. Wei, H. Zhou, Q. Gu and J. Xu, Identification of a binding site on soluble RANKL that can be targeted to inhibit soluble rank–RANKL interactions and treat osteoporosis. *Nat. Commun.* **13** (2022) 5338.

[14] J.B. Regard, N. Cherman, D. Palmer, S.A. Kuznetsov, F.S. Celi, J.-M. Guettier, M. Chen, N. Bhattacharyya, J. Wess, S.R. Coughlin, L.S. Weinstein, M.T. Collins, P.G. Robey and Y. Yang, Wnt/β-catenin signaling is differentially regulated by gα proteins and contributes to fibrous dysplasia. *Proc. Natl. Acad. Sci. U.S.A.* **108** (2011) 20101–20106.

[15] N. Bhattacharyya, M. Wiench, C. Dumitrescu, B.M. Connolly, T.H. Bugge, H.V. Patel, R.I. Gafni, N. Cherman, M. Cho, G.L. Hager and M.T. Collins, Mechanism of fgf23 processing in fibrous dysplasia. *J. Bone Miner. Res.* **27** (2012) 1132–1141.

[16] C. Hopkins, L.F. de Castro, A. Corsi, A. Boyce, M.T. Collins, M. Riminucci and A.-M. Heegaard, Fibrous dysplasia animal models: a systematic review. *Bone* **155** (2022) 116270.

[17] J.M. Whitlock, L.F. de Castro, M.T. Collins, L.V. Chernomordik and A.M. Boyce, An inducible explant model of osteoclast–osteoprogenitor coordination in exacerbated osteoclastogenesis. *iScience* **26** (2023) 1064703.

[18] L.F. De Castro, A.B. Burke, H.D. Wang, J. Tsai, P. Florenzano, K.S. Pan, N. Bhattacharyya, A.M. Boyce, R.I. Gafni, A.A. Molinolo, P.G. Robey and M.T. Collins, Activation of RANK/RANKL/OPG pathway is involved in the pathophysiology of fibrous dysplasia and associated with disease burden. *J. Bone Miner. Res.* **34** (2019) 290–294.

[19] P. Pivonka, J. Zimak, D.W. Smith, B.S. Gardiner, C.R. Dunstan, N.A. Sims, T. John Martin and G.R. Mundy, Model structure and control of bone remodeling: a theoretical study. *Bone* **43** (2008) 249–263.

[20] I. Ait Oumghar, A. Barkaoui and P. Chabrand, Toward a mathematical modeling of diseases' impact on bone remodeling: Technical review.*Front. Bioeng. Biotechnol.* **8** (2020).

[21] S. Trichilo and P. Pivonka, Application of Disease System Analysis to Osteoporosis: From Temporal to Spatio-Temporal Assessment of Disease Progression and Intervention. Springer International Publishing, Cham (2018) 61–121.

[22] J.L. Calvo-Gallego, P. Pivonka, R. Ruiz-Lozano and J. Martínez-Reina, Mechanistic PK–PD model of alendronate treatment of postmenopausal osteoporosis predicts bone site-specific response. *Front. Bioeng. Biotechnol.* **10** (2022) 940620.

[23] X. Zhao, P. Deng, R. Iglesias-Bartolome, P. Amornphimoltham, D.J. Steffen, Y. Jin, A.A. Molinolo, L.F. De Castro, D. Ovejero, Q. Yuan, Q. Chen, X. Han, D. Bai, S.S. Taylor, Y. Yang, M.T. Collins and J.S. Gutkind, Expression of an active $G\alpha_s$ mutant in skeletal stem cells is sufficient and necessary for fibrous dysplasia initiation and maintenance. *Proc. Natl. Acad. Sci. U.S.A.* **115** (2018) E428–E437.

[24] B. Palmisano, R. Labella, S. Donsante, C. Remoli, E. Spica, I. Coletta, G. Farinacci, M. Dello Spedale Venti, I. Saggio, M. Serafini, P.G. Robey, A. Corsi and M. Riminucci, Gsαr201c and estrogen reveal different subsets of bone marrow adiponectin expressing osteogenic cells. *Bone Res.* **10** (2022) 50.

[25] X. Chen, X. Zhi, J. Wang and J. Su, Rankl signaling in bone marrow mesenchymal stem cells negatively regulates osteoblastic bone formation. *Bone Res.* **6** (2018) 34.

[26] Y. Ikebuchi, S. Aoki, M. Honma, M. Hayashi, Y. Sugamori, M. Khan, Y. Kariya, G. Kato, Y. Tabata, J.M. Penninger, N. Udagawa, K. Aoki and H. Suzuki, Coupling of bone resorption and formation by RANKL reverse signalling. *Nature* **561** (2018) 195–200.

[27] A. Salhotra, H.N. Shah, B. Levi and M.T. Longaker, Mechanisms of bone development and repair. *Nat. Rev. Mol. Cell Biol.* **21** (2020) 696–711.

[28] W. Sohn, M.A. Simiens, K. Jaeger, S. Hutton and G. Jang, The pharmacokinetics and pharmacodynamics of denosumab in patients with advanced solid tumours and bone metastases: a systematic review. *Br. J. Clin. Pharmacol.* **78** (2014) 477–487.

[29] L. Wang, X. You, L. Zhang, C. Zhang and W. Zou, Mechanical regulation of bone remodelling. *Bone Res.* **10** (2022) 16.

[30] A. Raue, C. Kreutz, T. Maiwald, J. Bachmann, M. Schilling, U. Klingmüller and J. Timmer, Structural and practical identifiability analysis of partially observed dynamical models by exploiting the profile likelihood. *Bioinformatics* **25** (2009) 1923–1929.

[31] P.J. Marie, C. de Pollak, P. Chanson and A. Lomri, Increased proliferation of osteoblastic cells expressing the activating GS alpha mutation in monostotic and polyostotic fibrous dysplasia. *Am. J. Pathol.* **150** (1997) 1059–1069.

[32] T. Xiao, Y. Fu, W. Zhu, R. Xu, L. Xu, P. Zhang, Y. Du, J. Cheng and H. Jiang, HDAC8, a potential therapeutic target, regulates proliferation and differentiation of bone marrow stromal cells in fibrous dysplasia. *Stem Cells Transl. Med.* **8** (2018) 148–161.

[33] S.L. Teitelbaum, Bone resorption by osteoclasts. *Science* **289** (2000) 1504–1508.

[34] S.K. Verma, L.V. Chernomordik and K. Melikov, An improved metrics for osteoclast multinucleation. *Sci. Rep.* **8** (2018) 1768.

[35] J.S. Lee, E.J. FitzGibbon, Y.R. Chen, H.J. Kim, L.R. Lustig, S.O. Akintoye, M.T. Collins and L.B. Kaban, Clinical guidelines for the management of craniofacial fibrous dysplasia. *Orphanet J. Rare Dis.* **7** (2012) S2.

[36] P. Romanet, P. Philibert, F. Fina, T. Cuny, C. Roche, L. Ouafik, F. Paris, R. Reynaud and A. Barlier, Using digital droplet polymerase chain reaction to detect the mosaic ¡em¿gnas¡/em¿ mutations in whole blood DNA or circulating cell-free DNA in fibrous dysplasia and Mccune–Albright syndrome. *J. Pediatr.* **205** (2019) 281–285.e4.

[37] L.F. de Castro, Z. Michel, K. Pan, J. Taylor, V. Szymczuk, S. Paravastu, B. Saboury, G.Z. Papadakis, X. Li, K. Milligan, B. Boyce, S.M. Paul, M.T. Collins and A.M. Boyce, Safety and efficacy of denosumab for fibrous dysplasia of bone. *N. Engl. J. Med.* **388** (2023) 766–768.

[38] A. Saltelli, P. Annoni, I. Azzini, F. Campolongo, M. Ratto and S. Tarantola, Variance based sensitivity analysis of model output. Design and estimator for the total sensitivity index. *Comput. Phys. Commun.* **181** (2010) 259–270.

Appendix A. Comprehensive model definition

With reference to Figure 2 and the model of equation (2.1), we have considered a logistic behavior for the inhibitory effects. Nevertheless, a more comprehensive formulation that encompasses other inhibitory forms is as follows:

$$\frac{\mathrm{d}P}{\mathrm{d}t} = \rho P F_w + \hat{\rho}_S\, G_w - \alpha P - \delta_m P P_m, \tag{A.1a}$$

$$\frac{\mathrm{d}P_m}{\mathrm{d}t} = \rho_m P_m F_m + \hat{\rho}_{S_m}\, G_m, \tag{A.1b}$$

$$\frac{\mathrm{d}P_p}{\mathrm{d}t} = \rho_p P_p F_p + \delta_m P P_m, \tag{A.1c}$$

$$\frac{\mathrm{dC}_I}{\mathrm{d}t} = \alpha P - \delta C_I C_L, \tag{A.1d}$$

$$\frac{\mathrm{dC}_L}{\mathrm{d}t} = (\hat{\boldsymbol{\rho}}_C \cdot \boldsymbol{M})\, H - \gamma_C C_L, \tag{A.1e}$$

$$\frac{\mathrm{d}T}{\mathrm{d}t} = -\delta_T T\, (\mathbf{1} \cdot \boldsymbol{M}) - \gamma_T T, \tag{A.1f}$$

with $F_w \overset{\text{def}}{=} F_w(\boldsymbol{\lambda}, \boldsymbol{L}, \gamma_P)$, $F_m \overset{\text{def}}{=} F_m(\boldsymbol{\lambda}_m, \boldsymbol{L}, \gamma_{P_m})$, $F_p \overset{\text{def}}{=} F_p(\boldsymbol{\lambda}_p, \boldsymbol{L}, \gamma_{P_p})$, $G_w \overset{\text{def}}{=} G_w(\boldsymbol{\mu}, H\boldsymbol{M})$, $G_m \overset{\text{def}}{=} G_m(\boldsymbol{\mu}_m, H\boldsymbol{M})$, $H \overset{\text{def}}{=} H(\mu_T, T)$, $\boldsymbol{M} = (P, P_m, P_p, C_I)$, $\mathbf{1}$ is the four dimensional unit vector, $\cdot$ denotes the scalar product, and $\boldsymbol{L} = (P, P_m, P_p, C_I, C_L)$. Here, F_w, F_m, F_p, G_w and G_m represent carrying capacity functions that inhibit the proliferation and the flow of stem cells, respectively and $\hat{\boldsymbol{\rho}}_C, \boldsymbol{\lambda}, \boldsymbol{\lambda}_p, \boldsymbol{\lambda}_m, \boldsymbol{\mu}, \boldsymbol{\mu}_m$ are defined in Table A.1 together with their ranges. This inhibition is primarily due to the mechanical load produced by all cells in the culture plate and the RANKL protein secreted by the osteoblastic cells. The function H represents the PD component, controlling RANKL inhibition. Under normal conditions, ρ, ρ_m and ρ_p are the proliferation rates, γ_P, γ_{P_m} and γ_{P_p} are the degradation rates, $\hat{\rho}_S$ and $\hat{\rho}_{S_m}$ are the stem cells input rates, α is the differentiation rate, δ is the bone resorption rate, $\hat{\boldsymbol{\rho}}_C$ is the activation rate, γ_C is the deactivation rate, $\boldsymbol{\lambda}$, $\boldsymbol{\lambda}_m$, and $\boldsymbol{\lambda}_p$ are the proliferation inhibition coefficients, $\boldsymbol{\mu}$ and $\boldsymbol{\mu}_m$ are the stem cell inhibition coefficients, δ_m is the mutant conversion rate from P to P_p, δ_T is the RANKL-treatment binding rate, γ_T is the RANKL-treatment degradation rate, and μ_T is the RANKL-treatment inhibition coefficient. Also, in Appendices C and D, reduced versions of the above model, only for WT and in the presence of FD, respectively, are provided for completeness, together with their analysis.

A.1 Inhibitory and PD functions

The functions F and G must be chosen with care to accurately capture the inhibitory effects exerted by each signal. This selection is crucial, as it can lead to intricate solutions that may be challenging to justify within a biological context. Furthermore, these inhibitory effects depend on the specific conditions of the biological assay. We propose the following two alternative sets of functions to succinctly describe bone remodeling

$$F_1 = \frac{1}{1 + \boldsymbol{a} \cdot \boldsymbol{x}} - \gamma, \tag{A.2a}$$

$$G_1 = \frac{1}{1 + \boldsymbol{b} \cdot \boldsymbol{y}}, \tag{A.2b}$$

$$H_1 = \frac{1}{1 + cz}, \tag{A.2c}$$

TABLE A.1. Parameter definitions for the model of equation (A.1). Ranges estimated from numerical simulations (see Sect. 3.7). Rate units: day^{-1}. Coefficient units: dimensionless.

	Description	MM	LOG
ρ, ρ_m, ρ_p	Baseline proliferation rates	$(\alpha+\gamma_P, 24]$	$(\alpha, 24]$
$\boldsymbol{\lambda} = (\lambda_P, \lambda_{P_m}, \lambda_{P_p}, \lambda_{C_I}, \lambda_{C_L})$	Proliferation inhibition coefficients	$(0, 1]$	$(0, 1]$
$\boldsymbol{\lambda}_m = (\lambda_{m_P}, \lambda_{m_{P_m}}, \lambda_{m_{P_p}}, \lambda_{m_{C_I}}, \lambda_{m_{C_L}})$	Mutant proliferation inhibition coefficients	$(0, \lambda)$	$(0, \lambda)$
$\boldsymbol{\lambda}_p = (\lambda_{p_P}, \lambda_{p_{P_m}}, \lambda_{p_{P_p}}, \lambda_{p_{C_I}}, \lambda_{p_{C_L}})$	Phenocopied proliferation inhibition coefficients	$(0, \lambda)$	$(0, \lambda)$
α	WT differentiation rate	$(0, \rho-\gamma_P)$	$(0, \rho)$
γ_P	WT degradation rate	$(0, \rho-\alpha)$	–
γ_{P_m}	FD degradation rate	$(0, \rho_m)$	–
γ_{P_p}	Phenocopied FD degradation rate	$(0, \rho_p)$	–
$\hat{\rho}_S$	Stem cells net flow rate	$(0, \rho)$	$(0, \rho)$
$\hat{\rho}_{S_m}$	Mutant stem cells net flow rate	$(0, \rho_m)$	$(0, \rho_m)$
$\boldsymbol{\mu} = (\mu_P, \mu_{P_m}, \mu_{P_p}, \mu_{C_I})$	Stem cell inhibition coefficients	$(0, 1]$	$(0, 1]$
$\boldsymbol{\mu}_m = (\mu_{m_P}, \mu_{m_{P_m}}, \mu_{m_{P_p}}, \mu_{m_{C_I}})$	Mutant stem cell inhibition coefficients	$(0, 1]$	$(0, 1]$
δ	Bone resorption rate	$(0, 1]$	$(0, 1]$
$\hat{\boldsymbol{\rho}}_C = (\hat{\rho}_{C_P}, \hat{\rho}_{C_{P_m}}, \hat{\rho}_{C_{P_p}}, \hat{\rho}_{C_{C_I}})$	Osteoclast activation rates	$(0, 1]$	$(0, 1]$
γ_C	Osteoclast deactivation rate	$(0, 1]$	$(0, 1]$
δ_m	Mutant conversion rate	$(0, 1]$	$(0, 1]$
δ_T	Treatment binding rate	$(0, 1]$	$(0, 1]$
γ_T	Treatment degradation rate	$(0, 1]$	$(0, 1]$
μ_T	Treatment's regulator coefficient	$(0, 1]$	$(0, 1]$

and

$$F_2 = (1 - \boldsymbol{a}\cdot\boldsymbol{x})_+ , \tag{A.3a}$$

$$G_2 = (1 - \boldsymbol{b}\cdot\boldsymbol{y})_+ , \tag{A.3b}$$

$$H_2 = (1 - cz)_+ , \tag{A.3c}$$

where $\boldsymbol{a}, \boldsymbol{b} \in \mathbb{R}^n$ and $c \in \mathbb{R}^+$ are the carrying capacity coefficients, $\boldsymbol{x}, \boldsymbol{y} \in \mathbb{R}^n$ are the populations involved in the inhibition, $\gamma \in \mathbb{R}^+$ being a dimensionless decay term, conveniently utilized to guarantee boundedness of the solutions, and n the number of populations. Specifically in our ODE model, in $\mathrm{d}P/\mathrm{d}t$, $\mathrm{d}P_m/\mathrm{d}t$ and $\mathrm{d}P_p/\mathrm{d}t$, $\boldsymbol{a}$ will comprise $\boldsymbol{\lambda}$, $\boldsymbol{\lambda_m}$, and $\boldsymbol{\lambda_p}$, $\boldsymbol{b}$ will comprise $\boldsymbol{\mu}$ and $\boldsymbol{\mu_m}$, c will be $\boldsymbol{\mu_T}$, $\boldsymbol{x}$ will be $\boldsymbol{L}$, $\boldsymbol{y}$ will be $H\boldsymbol{M}$, z will be T, and γ will comprise γ_P, γ_{P_m}, and γ_{P_p}. Functions (A.2) display a Hill or Michaelis–Menten (MM) form, while functions (A.3) are modified logistic functions (LOG), since both $\boldsymbol{L}$ and $\boldsymbol{M}$ contain P, P_m or P_p, respectively. Furthermore, to preclude biologically inconsistent behaviors such as reverse proliferation or reverse differentiation, only the positive part of these functions will be considered.

Henceforth, the parameters $\boldsymbol{\lambda}$, $\boldsymbol{\mu}$ and $\hat{\boldsymbol{\rho}}_C$ will be regarded as scalars, indicating that each signal or coefficient exerts a uniform effect across all cell populations. Accordingly, when the MM inhibition functions (A.2) are incorporated into the treatment model (A.1), the resulting system reads as follows

$$\frac{\mathrm{d}P}{\mathrm{d}t} = \frac{\rho P}{1+\lambda L} + \frac{\hat{\rho}_S}{1+\mu M_2} - (\alpha+\gamma_P)P - \delta_m P P_m, \tag{A.4a}$$

$$\frac{\mathrm{d}P_m}{\mathrm{d}t} = \frac{\rho_m P_m}{1+\lambda_m L} + \frac{\hat{\rho}_{S_m}}{1+\mu_m M_2} - \gamma_{P_m} P_m, \tag{A.4b}$$

$$\frac{\mathrm{d}P_p}{\mathrm{d}t} = \frac{\rho_p P_p}{1+\lambda_p L} + \delta_m P P_m - \gamma_{P_p} P_p, \tag{A.4c}$$

$$\frac{\mathrm{d}C_I}{\mathrm{d}t} = \alpha P - \delta C_I C_L, \tag{A.4d}$$

$$\frac{\mathrm{d}C_L}{\mathrm{d}t} = \hat{\rho}_C M_2 - \gamma_C C_L, \tag{A.4e}$$

$$\frac{\mathrm{d}T}{\mathrm{d}t} = -\delta_T T N - \gamma_T T, \tag{A.4f}$$

with $N = P + P_m + P_p + C_I, M_2 = N/(1 + \mu_T T)$, and $L = P + P_m + P_p + C_I + C_L$. The same assumptions transform the model, through equation (A.1), with the LOG inhibition functions (A.3), resulting in the equation (2.1). Note that γ_P, γ_{P_m}, and γ_{P_p} are not required in the logistic form as they can be absorbed into other global constants.

Appendix B. Model properties

B.1 Existence, boundedness and positivity of solutions

Theorem B.1. *Consider the following set*

$$Q = \{(P, P_m, P_p, C_I, C_L, T) \in \mathbb{R}^6 : P, P_m, P_p, C_I, C_L, T > 0\}, \tag{B.1}$$

and the initial values in Q

$$\begin{aligned} P(t_0) = P^0, P_m(t_0) = P_m^0, P_p(t_0) = P_p^0, \\ C_I(t_0) = C_I^0, C_L(t_0) = C_L^0, T(t_0) = T^0. \end{aligned} \tag{B.2}$$

Then, the initial value problem for equations (2.1) *and* (A.4) *has a unique local-in-time solution for each* $t \in [t_0 - \epsilon, t_0 + \epsilon]$, *for some value* $\epsilon > 0$.

Proof. The existence of a solution for systems (2.1) and (A.4) is guaranteed for each $(P, P_m, P_p, C_I, C_L, T) \in Q$ by continuity of their right-hand-side functions. The fact that the partial derivatives of such functions are continuous and finite implies they are locally Lipschitz continuous. Therefore, by the Picard–Lindelöf theorem, the solutions of systems (2.1) and (A.4) with initial values (B.2) are unique and local-in-time. □

Theorem B.2. *The solutions of equation* (A.4) *with positive initial values* $(P^0, P_m^0, P_p^0, C_I^0, C_L^0, T^0) \in Q$ *are positive.*

Proof. First, we will show the positivity of P in Q. Consider its equation in (A.4). Then,

$$\begin{aligned} \frac{\mathrm{d}P}{\mathrm{d}t} &= \frac{\rho P}{1 + \lambda L} + \frac{\hat{\rho}_S}{1 + \mu M_2} - (\alpha + \gamma_P)P - \delta_m P P_m \\ &> -(\alpha + \gamma_P + \delta_m P_m)P \stackrel{\text{def}}{=} -\beta(t)P. \end{aligned} \tag{B.3}$$

By Grönwall's lemma it follows that

$$P(t) > P^0 \mathrm{e}^{-\int_{t_0}^{t} \beta(s)\mathrm{d}s} \geq 0. \tag{B.4}$$

The same procedure can be applied to $P_m(t), P_p(t), C_I(t), C_L(t)$ and $T(t)$. This completes the proof. □

Theorem B.3. *The solutions of equation* (2.1) *with* $(P^0, P_m^0, P_p^0, C_I^0, C_L^0, T^0) \in Q$ *are positive.*

Proof. The proof is analogous to the previous theorem using again Grönwall's lemma. □

Theorem B.4. *The solutions of equation* (A.4) *with* $(P^0, P_m^0, P_p^0, C_I^0, C_L^0, T^0) \in Q$ *are bounded.*

Proof. We start by considering the equation $\dfrac{\mathrm{d}T}{\mathrm{d}t} = -\delta_T T N - \gamma_T T$. By Theorem B.2, it follows that $\mathrm{d}T/\mathrm{d}t < 0$ for all $t \geq t_0$ because $N(t)$ and $T(t)$ are positive. Therefore, T is bounded from above by $T^0 \in Q$.

Next, we show that $P = P(t)$ is bounded. From equation (A.4a), we have

$$\begin{aligned}\frac{\mathrm{d}P}{\mathrm{d}t} &= \frac{\rho P}{1+\lambda L} + \frac{\hat{\rho}_S}{1+\mu M_2} - (\alpha+\gamma_P)P - \delta_m P P_m \\ &< \frac{\rho P}{1+\lambda P} + \frac{\hat{\rho}_S\,(1+\mu_T T)}{1+\mu P} - (\alpha+\gamma_P)P \\ &< \frac{\rho}{\lambda} + \hat{\rho}_S\left(1+\mu_T T^0\right) - (\alpha+\gamma_P)P, \end{aligned} \tag{B.5}$$

where we have used again Theorem B.2, and thus $\dfrac{\rho P}{1+\lambda L} < \dfrac{\rho P}{1+\lambda P} < \dfrac{\rho}{\lambda}$, together with $\dfrac{\hat{\rho}_S}{1+\mu M_2} < \dfrac{\hat{\rho}_S\,(1+\mu_T T)}{1+\mu P} < \hat{\rho}_S\left(1+\mu_T T^0\right)$, which are finite positive constants. Therefore, setting the constant $P^{(*)} \stackrel{\text{def}}{=} \dfrac{\rho}{\lambda} + \hat{\rho}_S\left(1+\mu_T T^0\right)$, we get from (B.5)

$$\begin{aligned}&\frac{\mathrm{d}P}{\mathrm{d}t} < P^{(*)} - (\alpha+\gamma_P)P \implies \\ &P < \frac{P^{(*)}}{\alpha+\gamma_P} + \left(P^0 - \frac{P^{(*)}}{\alpha+\gamma_P}\right)\mathrm{e}^{-(\alpha+\gamma_P)(t-t_0)} \stackrel{\text{def}}{=} B(t) \leq B^{(*)} < \infty, \end{aligned} \tag{B.6}$$

where we have employed Grönwall's lemma and defined an upper positive finite constant $B^{(*)}$. Hence, P is bounded.

Analogously, P_m and P_p are also bounded, since

$$\frac{\mathrm{d}P_m}{\mathrm{d}t} < P_m^{(*)} - \gamma_{P_m} P_m \implies P_m < c_m \mathrm{e}^{-\gamma_{P_m}(t-t_0)} + \frac{P_m^{(*)}}{\gamma_{P_m}} \stackrel{\text{def}}{=} B_m(t) \leq B_m^{(*)} < \infty, \tag{B.7}$$

and

$$\begin{aligned}&\frac{\mathrm{d}P_p}{\mathrm{d}t} < P_p^{(*)} + \delta_m P P_m - \gamma_{P_p} P_p < P_p^{(*)} + \delta_m B^{(*)} B_m^{(*)} - \gamma_{P_p} P_p \implies \\ &P_p < c_p \mathrm{e}^{-\gamma_{P_p}(t-t_0)} + \frac{P_p^{(*)} + \delta_m B^{(*)} B_m^{(*)}}{\gamma_{P_p}} \stackrel{\text{def}}{=} B_p(t) \leq B_p^{(*)} < \infty, \end{aligned} \tag{B.8}$$

where $P_m^{(*)}$ and $P_p^{(*)}$ are upper positive finite constants, defined in a similar manner as $P^{(*)}$, whereas c_m and c_p are integration constants.

We now consider equations (A.4d) and (A.4e). Since we have shown that $P < B^{(*)}$ and also, $M_2 = N/(1+\mu_T T) < N = P + P_m + P_p + C_I < B^{(*)} + B_m^{(*)} + B_p^{(*)} + C_I$, then

$$\frac{\mathrm{d}C_I}{\mathrm{d}t} < C_I^{(*)} - \delta C_I C_L, \tag{B.9a}$$

$$\frac{\mathrm{d}C_L}{\mathrm{d}t} < C_L^{(*)} + \hat{\rho}_C C_I - \gamma_C C_L, \tag{B.9b}$$

where, for convenience, we have defined the positive constants $C_I^{(*)} = \alpha B^{(*)}$ and $C_L^{(*)} = \hat{\rho}_C\left(B^{(*)} + B_m^{(*)} + B_p^{(*)}\right)$. First, observe from (B.9a) that C_I and C_L cannot both be unbounded. If they were, the term $C_I C_L$ would grow arbitrarily large, causing $\dfrac{\mathrm{dC}_I}{\mathrm{d}t}$ to eventually become negative for sufficiently large t. This would force C_I to decrease, thereby preventing its unbounded growth. Hence, at least one of C_I or C_L must remain bounded.

To establish boundedness rigorously, assume for contradiction that C_L is unbounded. Then, for inequality (B.9b) to hold, C_I would also need to be unbounded. However, this leads to a contradiction since C_I and C_L cannot both be unbounded. Therefore, C_L must be bounded. Next, suppose there exists a constant $m_L > 0$ such that $C_L \geq m_L$ for all $t \geq t_0$. Using this lower bound into inequality (B.9a), we obtain

$$\frac{\mathrm{dC}_I}{\mathrm{d}t} < C_I^{(*)} - \delta C_I C_L \leq C_I^{(*)} - \delta m_L C_I, \tag{B.10}$$

where the last inequality follows from the fact that C_L is continuous and positive for all $t \geq t_0$. Multiplying both sides of this inequality by the integrating factor $\mathrm{e}^{\delta m_L t}$ gives

$$\frac{\mathrm{d}}{\mathrm{d}t}\left(C_I \mathrm{e}^{\delta m_L t}\right) < C_I^{(*)} \mathrm{e}^{\delta m_L t}. \tag{B.11}$$

Integrating both sides and rearranging yields

$$C_I < C_I^0 \mathrm{e}^{-\delta m_L t} + \frac{C_I^{(*)}}{\delta m_L}\left(1 - \mathrm{e}^{-\delta m_L t}\right) \stackrel{\text{def}}{=} B_I(t) \leq B_I^{(*)} < \infty, \tag{B.12}$$

which proves that C_I is bounded.

Finally, we note that if no $m_L > 0$ exists such that $C_L \geq m_L$ for all $t \geq t_0$, then the boundedness of C_I remains to be established through a separate argument. However, as shown above, if $m_L > 0$ does exists, both C_I and C_L are indeed bounded. □

Theorem B.5. *The solutions of equation (2.1) with $(P^0, P_m^0, P_p^0, C_I^0, C_L^0, T^0) \in Q$ are bounded.*

Proof. Collecting P_m from equation (2.1b) when $1 - \lambda_m L > 0$ and $1 - \mu_m M > 0$,

$$\begin{aligned}\frac{\mathrm{d}P_m}{\mathrm{d}t} = &-\rho_m \lambda_m P_m^2 + (\rho_m(1 - \lambda_m(P + P_p + C_I + C_L)) - \mu_m \hat{\rho}_{S_m}) P_m \\ &+ \hat{\rho}_{S_m}(1 - \mu_m(P + P_p + C_I)) \stackrel{\text{def}}{=} a_m P_m^2 + b_m(t) P_m + c_m(t),\end{aligned} \tag{B.13}$$

where $a_m, b_m(t), c_m(t) \in \mathbb{R}$ and $a_m < 0$. Note that the boundedness of $b_m(t)$ and $c_m(t)$ implies the boundedness of P_m. Hence, due to the positivity of F_2 and G_2 in equation (A.3),

$$1 - \lambda_m L > 0 \implies 1 > 1 - \lambda_m(P + P_p + C_I + C_L) > \lambda_m P_m > 0, \tag{B.14}$$

$$1 - \mu_m M > 0 \implies 1 > 1 - \mu_m(P + P_p + C_I) > \mu_m P_m > 0, \tag{B.15}$$

therefore,

$$-\mu_m \hat{\rho}_{S_m} < \lambda_m P_m - \mu_m \hat{\rho}_{S_m} < b_m(t) < \rho_m - \mu_m \hat{\rho}_{S_m}, \tag{B.16}$$

$$0 < c_m(t) < \hat{\rho}_S. \tag{B.17}$$

thus, P_m is bounded when $1 - \lambda_m L > 0$ and $1 - \mu_m M > 0$. Analogously, when $1 - \lambda_m L \leq 0$ or $1 - \mu_m M \leq 0$, then, respectively, $(1 - \lambda_m L)_+ = 0$ or $(1 - \mu_m M)_+ = 0$, which imply that P_m is bounded, either way.

Following the same procedure, collecting P_p from equation (2.1c),

$$\frac{\mathrm{d}P_p}{\mathrm{d}t} = -\rho_p \lambda_p P_p^2 + (\rho_p(1 - \lambda_p(P + P_m + C_I + C_L)))P_p \stackrel{\text{def}}{=} a_p P_p^2 + b_p(t)P_p, \tag{B.18}$$

where $a_p, b_p(t) \in \mathbb{R}$ and $a_p < 0$. Considering F_2 and G_2 as before,

$$1 > 1 - \lambda_m(P + P_m + C_I + C_L) > \lambda_m P_p > 0, \tag{B.19}$$

$$0 < \lambda_p P_p < b(t) < \rho_p, \tag{B.20}$$

thus, P_p is bounded, too.

Finally, collecting P from

$$\begin{aligned}\frac{\mathrm{d}P}{\mathrm{d}t} = -\rho\lambda P^2 + (\rho(1 - \lambda(P_m + P_p + C_I + C_L)) - \alpha - \mu\hat{\rho}_S - \delta_m P_m)P \\ + \hat{\rho}_S(1 - \mu(P_m + P_p + C_I)) \stackrel{\text{def}}{=} aP^2 + b(t)P + c(t),\end{aligned} \tag{B.21}$$

where $a, b(t), c(t) \in \mathbb{R}$ and $a < 0$. Considering F_2 and G_2 as above,

$$1 > 1 - \lambda(P_m + P_p + C_I + C_L) > \lambda P, \tag{B.22}$$

$$1 > 1 - \mu(P_m + P_p + C_I) > \mu P, \tag{B.23}$$

$$-\alpha - \mu\hat{\rho}_S - \delta_m P_m < b(t) < \rho - \alpha - \mu\hat{\rho}_S - \delta_m P_m, \quad 0 < c(t) < \hat{\rho}_S, \tag{B.24}$$

thus, P is bounded, which implies that C_I and C_L are also bounded. □

Appendix C. Wild-type tissue

C.1 Model formulation

$$\frac{\mathrm{d}P}{\mathrm{d}t} = \rho P F_w + \hat{\rho}_S G_w - \alpha P, \tag{C.1a}$$

$$\frac{\mathrm{dC}_I}{\mathrm{d}t} = \alpha P - \delta C_I C_L, \tag{C.1b}$$

$$\frac{\mathrm{dC}_L}{\mathrm{d}t} = \hat{\boldsymbol{\rho}}_C \cdot \boldsymbol{M} - \gamma_C C_L, \tag{C.1c}$$

with $F_w \stackrel{\text{def}}{=} F_w(\boldsymbol{\lambda}, \boldsymbol{L}, \gamma_P)$, $G_w \stackrel{\text{def}}{=} G_w(\boldsymbol{\mu}, \boldsymbol{M})$, $\boldsymbol{M}^{\mathrm{T}} = (P, C_I)$, $\boldsymbol{L} = (P, C_I, C_L)$, $\hat{\boldsymbol{\rho}}_C = (\hat{\rho}_{C_P}, \hat{\rho}_{C_{C_I}})$, $\boldsymbol{\lambda} = (\lambda_P, \lambda_{C_I}, \lambda_{C_L})$ and $\boldsymbol{\mu} = (\mu_P, \mu_{C_I})$. F_w and G_w represent carrying capacity functions that inhibit the proliferation and the flow of stem cells, ρ, γ_P, $\hat{\rho}_S$, α, δ, $\hat{\boldsymbol{\rho}}_C$, γ_C, $\boldsymbol{\lambda}$, $\boldsymbol{\mu}$ are defined in Table A.1.

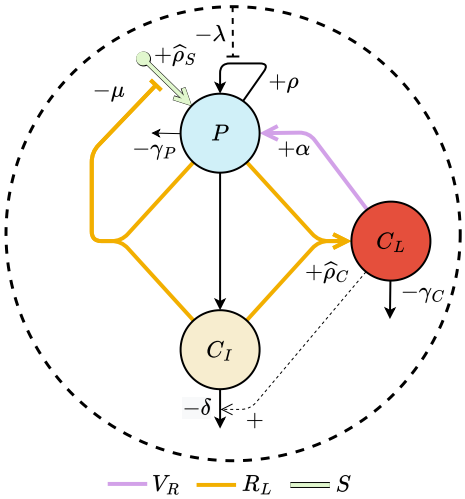

FIGURE C.1. Schematic representation of the WT tissue model. The boundary of the culture (C_P) inhibits ($-\lambda$) proliferation ($+\rho$) and vesicular rank (V_R) promotes differentiation ($+\alpha$). RANKL (R_L) is secreted by osteoprogenitors (P) and osteocytes (C_I) to promote osteoclast (C_L) activation ($+\hat{\rho}_C$) and inhibit ($-\mu$) the mesenchymal stem cells flow (S). Bone matrix is degraded ($-\delta$) by C_L, since it is proportional to C_I.

C.2 LOG inhibition

$$\frac{\mathrm{d}P}{\mathrm{d}t} = \rho P(1-\lambda L)_+ + \hat{\rho}_S(1-\mu M_1)_+ - \alpha P, \tag{C.2a}$$

$$\frac{\mathrm{dC}_I}{\mathrm{d}t} = \alpha P - \delta C_I C_L, \tag{C.2b}$$

$$\frac{\mathrm{dC}_L}{\mathrm{d}t} = \hat{\rho}_C M_1 - \gamma_C C_L, \tag{C.2c}$$

with $M_1 = P + C_I$ and $L = P + C_I + C_L$.

C.3 MM inhibition

$$\frac{\mathrm{d}P}{\mathrm{d}t} = \frac{\rho P}{1+\lambda L} + \frac{\hat{\rho}_S}{1+\mu M_2} - (\alpha+\gamma_P)P, \tag{C.3a}$$

$$\frac{\mathrm{dC}_I}{\mathrm{d}t} = \alpha P - \delta C_I C_L, \tag{C.3b}$$

$$\frac{\mathrm{dC}_L}{\mathrm{d}t} = \hat{\rho}_C M_2 - \gamma_C C_L, \tag{C.3c}$$

with $M_2 = P + C_I$ and $L = P + C_I + C_L$.

C.4 Existence, boundedness and positivity of solutions

Theorem C.1. *Considering the following set*

$$Q = \{(P, C_I, C_L) \in \mathbb{R}^3 : P, C_I, C_L > 0\}, \tag{C.4}$$

and the initial values in Q

$$P(t_0) = P^0, C_I(t_0) = C_I^0, C_L(t_0) = C_L^0, \tag{C.5}$$

then, the initial value problem for either equations (C.3) *and* (C.2) *has a unique local-in-time solution for each* $t \in [t_0 - \epsilon, t_0 + \epsilon]$*, for some value* $\epsilon > 0$.

Proof. The existence of a solution for systems (C.3) and (C.2) is guaranteed for each $(P, C_I, C_L) \in Q$ by continuity of their right hand side functions. The fact that the partial derivatives of such functions are continuous and finite implies they are locally Lipschitz continuous. Therefore, by the Picard–Lindelöf theorem the solutions of systems (C.3) and (C.2) with initial values (C.5) are unique and local-in-time. □

Theorem C.2. *The solutions of equation* (C.3) *with* $(P^0, C_I^0, C_L^0) \in Q$ *are positive.*

Proof. Following the same procedure of Theorem B.2,

$$\frac{\mathrm{d}P}{\mathrm{d}t} > -(\alpha + \gamma_P)P \implies P > P^0 \mathrm{e}^{-(\alpha+\gamma_P)t} > 0, \tag{C.6a}$$

$$\frac{\mathrm{dC}_I}{\mathrm{d}t} > -\delta C_I C_L \implies C_I > C_I^0 \mathrm{e}^{-\delta \int_{t_0}^{t} C_L \,\mathrm{d}t} > 0, \tag{C.6b}$$

$$\frac{\mathrm{dC}_L}{\mathrm{d}t} > -\gamma_C C_L \implies C_L > C_L^0 \mathrm{e}^{-\gamma_C t} > 0. \tag{C.6c}$$

□

Theorem C.3. *The solutions of equation* (C.2) *with* $(P^0, C_I^0, C_L^0) \in Q$ *are positive.*

Proof. Following the same procedure of Theorem B.2,

$$\frac{\mathrm{d}P}{\mathrm{d}t} > -\alpha P \implies P > P^0 \mathrm{e}^{-\alpha t} > 0, \tag{C.7a}$$

$$\frac{C_I}{\mathrm{d}t} > -\delta C_I C_L \implies C_I > C_I^0 \mathrm{e}^{-\delta \int_{t_0}^{t} C_L \,\mathrm{d}t} > 0, \tag{C.7b}$$

$$\frac{\mathrm{dC}_L}{\mathrm{d}t} > -\gamma_C C_L \implies C_L > C_L^0 \mathrm{e}^{-\delta t} > 0. \tag{C.7c}$$

□

Theorem C.4. *The solutions of equation* (C.3) *with* $(P^0, C_I^0, C_L^0) \in Q$ *are bounded.*

Proof. Following the same procedure of Theorem B.4, letting $A(t) = \alpha + \gamma_P$,

$$\frac{\mathrm{d}P}{\mathrm{d}t} < \frac{\rho}{\lambda} - AP \implies P < c\mathrm{e}^{-At} + \frac{\rho}{\lambda A} \stackrel{\text{def}}{=} B(t), \tag{C.8}$$

hence, P is bounded, which implies that C_I and C_L are also bounded, by theorem B.4. □

Theorem C.5. *The solutions of equation* (C.2) *with* $(P^0, C_I^0, C_L^0) \in Q$ *are bounded.*

Proof. Following the same procedure of Theorem B.5, collecting P from

$$\begin{aligned}\frac{\mathrm{d}P}{\mathrm{d}t} =& -\rho\lambda P^2 + (\rho(1-\lambda(C_I+C_L)) - \alpha - \mu\hat{\rho}_S)P \\ &+ \hat{\rho}_S(1-\mu(C_I)) \stackrel{\text{def}}{=} aP^2 + b(t)P + c(t),\end{aligned} \tag{C.9}$$

where $a, b(t), c(t) \in \mathbb{R}$ and $a < 0$. Considering F_2 and G_2 as above,

$$1 > 1 - \lambda(C_I + C_L) > \lambda P, \tag{C.10}$$

$$1 > 1 - \mu(C_I) > \mu P, \tag{C.11}$$

and

$$-\alpha - \mu\hat{\rho}_S < b(t) < \rho - \alpha - \mu\hat{\rho}_S, \quad 0 < c(t) < \hat{\rho}_S, \tag{C.12}$$

thus, P is bounded when $1 - \lambda L > 0$ and $1 - \mu M_1 > 0$. Analogously, when $1 - \lambda L \leq 0$ or $1 - \mu M_1 \leq 0$, then, respectively, $(1 - \lambda L)_+ = 0$ or $(1 - \mu M_1)_+ = 0$, which imply that P is bounded, either way, which implies that C_I and C_L are also bounded. □

C.5 Steady states

The steady states for system (C.2) are

$$C_{I_i}^* = \frac{(\rho(1-\lambda(C_{L_i}^* + P_i^*)) - \alpha - \mu\hat{\rho}_S)P_i^* + \hat{\rho}_S}{\mu\hat{\rho}_S + \lambda\rho P_i^*}, \tag{C.13a}$$

$$C_{L_i}^* = \frac{b_{C_{L_i^*}} \pm \sqrt{{b_{C_{L_i^*}}}^2 - 4\delta\lambda\rho {P_i^*}^2(\alpha\lambda\rho P_i^* + \alpha\mu\hat{\rho}_S)}}{2\delta\lambda\rho P_i^*}, \tag{C.13b}$$

$$P_i^* \equiv a_P P^3 + b_P P^2 + c_P P + d_P = 0, \tag{C.13c}$$

$$b_{C_{L_i^*}} = \delta((\rho(1-\lambda P_i^*) - \alpha - \mu\hat{\rho}_S)P_i^* + \hat{\rho}_S), \tag{C.13d}$$

$$a_{P_i^*} = \lambda\rho(\gamma_C + \hat{\rho}_C)(\delta\hat{\rho}_C(\rho - \alpha) + \alpha\lambda\rho(\gamma_C + \hat{\rho}_C)), \tag{C.13e}$$

$$\begin{aligned}b_{P_i^*} =& \delta\hat{\rho}_C(((\lambda+\mu)\gamma_C + \lambda\hat{\rho}_C)\rho\hat{\rho}_S - \gamma_C(\rho^2 + \alpha^2)) \\ &+ \alpha\gamma_C(2\lambda\rho\mu\hat{\rho}_S(\gamma_C + \hat{\rho}_C) + \delta\hat{\rho}_C(2\rho - \mu\hat{\rho}_S)),\end{aligned} \tag{C.13f}$$

$$c_{P_i^*} = -\gamma_C\hat{\rho}_S(2\delta\hat{\rho}_C(\rho - \alpha) - \mu\hat{\rho}_S(\alpha\gamma_C\mu + \delta\hat{\rho}_C)), \tag{C.13g}$$

$$d_{P_i^*} = -\delta\gamma_C\hat{\rho}_C\hat{\rho}_S^2. \tag{C.13h}$$

C.6 Stability conditions

Having all positive parameters, from equation (C.13), it's easy to see that $d_{P_i^*} < 0$. Furthermore, considering the ranges shown in Table 1, if

$$\rho > \alpha, \tag{C.14a}$$

$$\mu\hat{\rho}_S < \frac{2\delta\hat{\rho}_C(\rho - \alpha)}{\alpha\gamma_C\mu + \delta\hat{\rho}_C}, \tag{C.14b}$$

then $a_{P_i^*} > 0$ and $c_{P_i^*} < 0$. Hence, by the Descartes' rule of signs, there is only 1 positive root. Considering the Jacobian matrix,

$$J = \begin{pmatrix} \rho(1-\lambda(L^*+P^*)) - \alpha - \mu\hat{\rho}_S & -\lambda\rho P^* - \mu\hat{\rho}_S & -\lambda\rho P^* \\ \alpha & -\delta C_L^* & -\delta C_I^* \\ \hat{\rho}_C & \hat{\rho}_C & -\gamma_C \end{pmatrix}, \tag{C.15}$$

then, the characteristic polynomial is a third grade polynomial defined as $\lambda_a x^3 + \lambda_b x^2 + \lambda_c x + \lambda_d = 0$ where:

$$\begin{aligned}
\lambda_a =& 1, && \text{(C.16a)}\\
\lambda_b =& \delta C_L^* + \gamma_C - (\rho(1-\lambda(P^*+L^*)) - \alpha - \mu\hat{\rho}_S), && \text{(C.16b)}\\
\lambda_c =& \lambda\rho((L^*+P^*)(C_L^*\delta+\gamma_C) + P^*(\hat{\rho}_C+\alpha)) - \gamma_C(\rho - \mu\hat{\rho}_S - (1+C_L^*\delta))\\
&+ \mu\hat{\rho}_S\alpha + \delta(C_I^*\hat{\rho}_C - C_L^*(\rho - \alpha - \mu\hat{\rho}_S)), && \text{(C.16c)}\\
\lambda_d =& \lambda\rho(\gamma_C(\delta(L^*+P^*)C_L^* + \alpha P^*) + \hat{\rho}_C(\delta(C_I^*L^* + C_L^*P^*) + \alpha P^*))\\
&- \delta(\gamma_C(\rho - \alpha - \mu\hat{\rho}_S)C_L^* + \hat{\rho}_C(\rho-\alpha)C_I^*), + \alpha\gamma_C\mu\hat{\rho}_S. && \text{(C.16d)}
\end{aligned}$$

We know that $\lambda_a > 0$, hence, $\lambda_b > 0$, $\lambda_c > 0$ and $\lambda_d > 0$ delimit a stability region where the critical state is stable. From Descartes' signs rule, the stability region has 3 real negatives or 1 real negative and 2 complex roots. In the latter case, the right semi-plane of the complex plane with the Routh–Hurtwitz criteria, it is found a stable subspace when:

$$\lambda_d < \lambda_b\lambda_c. \tag{C.17}$$

Appendix D. Dysplastic tissue

D.1 Model formulation

$$\begin{aligned}
\frac{\mathrm{d}P}{\mathrm{d}t} &= \rho P F_w + \hat{\rho}_S\, G_w - \alpha P - \delta_m P P_m, && \text{(D.1a)}\\
\frac{\mathrm{d}P_m}{\mathrm{d}t} &= \rho_m P_m F_m + \hat{\rho}_{S_m}\, G_m, && \text{(D.1b)}\\
\frac{\mathrm{d}P_p}{\mathrm{d}t} &= \rho_p P_p F_p + \delta_m P P_m, && \text{(D.1c)}\\
\frac{\mathrm{dC}_I}{\mathrm{d}t} &= \alpha P - \delta C_I C_L, && \text{(D.1d)}\\
\frac{\mathrm{dC}_L}{\mathrm{d}t} &= \hat{\boldsymbol{\rho}}_C \cdot \boldsymbol{M} - \gamma_C C_L, && \text{(D.1e)}
\end{aligned}$$

with $F_w \overset{\text{def}}{=} F_w(\boldsymbol{\lambda}, \boldsymbol{L}, \gamma_P)$, $F_m \overset{\text{def}}{=} F_m(\boldsymbol{\lambda}_m, \boldsymbol{L}, \gamma_{P_m})$, $F_p \overset{\text{def}}{=} F_p(\boldsymbol{\lambda}_p, \boldsymbol{L}, \gamma_{P_p})$, $G_w \overset{\text{def}}{=} G_w(\boldsymbol{\mu}, \boldsymbol{M})$, $G_m \overset{\text{def}}{=} G_m(\boldsymbol{\mu}_m, \boldsymbol{M})$, $\boldsymbol{M}^{\mathrm{T}} = (P, P_m, P_p, C_I)$, $\boldsymbol{L} = (P, P_m, P_p, C_I, C_L)$, $\hat{\boldsymbol{\rho}}_C = (\hat{\rho}_{C_P}, \hat{\rho}_{C_{P_m}}, \hat{\rho}_{C_{P_p}}, \hat{\rho}_{C_{C_I}})$, $\boldsymbol{\lambda} = (\lambda_P, \lambda_{P_m}, \lambda_{P_p}, \lambda_{C_I}, \lambda_{C_L})$ and $\boldsymbol{\mu} = (\mu_P, \mu_{P_m}, \mu_{P_p}, \mu_{C_I})$. F_w, F_m, F_p and G_w represent carrying capacity functions that inhibit the proliferation and the flow of stem cells, and ρ, ρ_m, ρ_p, γ_P, γ_{P_m}, γ_{P_p}, $\hat{\rho}_S$, $\hat{\rho}_{S_m}$, α, δ, $\hat{\boldsymbol{\rho}}_C$, γ_C, $\boldsymbol{\lambda}$, $\boldsymbol{\lambda}_m$, $\boldsymbol{\lambda}_p$, $\boldsymbol{\mu}$, $\boldsymbol{\mu}_m$, δ_m, δ_T, γ_T, μ_T are defined in Table A.1.

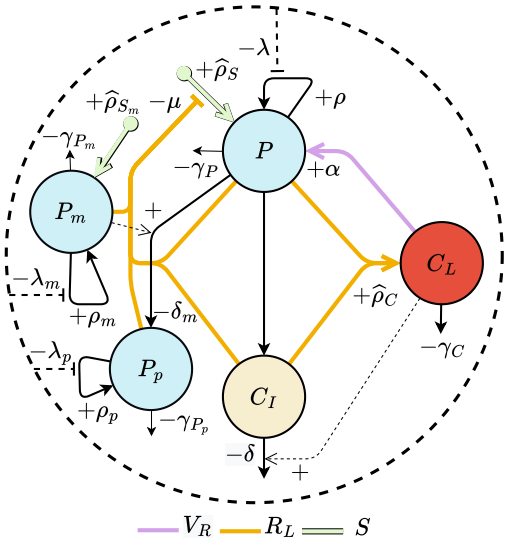

FIGURE D.1. Schematic representation of the dysplastic tissue model, based on Figure C.1. Mutant osteoprogenitors (P_m) behave similarly to P, but with impaired differentiation. Additionally, P_m converts ($-\delta_m$) WT osteoprogenitors (P) into phenotype-transferred osteoprogenitors (P_p), which mimic the behavior of P_m.

D.2 LOG inhibition

$$\frac{\mathrm{d}P}{\mathrm{d}t} = \rho P(1-\lambda L)_+ + \hat{\rho}_S(1-\mu M_1)_+ - \alpha P - \delta_m P P_m, \tag{D.2a}$$

$$\frac{\mathrm{d}P_m}{\mathrm{d}t} = \rho_m P_m(1-\lambda_m L)_+ + \hat{\rho}_{S_m}(1-\mu_m M_1)_+, \tag{D.2b}$$

$$\frac{\mathrm{d}P_p}{\mathrm{d}t} = \rho_p P_p(1-\lambda_p L)_+ + \delta_m P P_m, \tag{D.2c}$$

$$\frac{\mathrm{dC}_I}{\mathrm{d}t} = \alpha P - \delta C_I C_L, \tag{D.2d}$$

$$\frac{\mathrm{dC}_L}{\mathrm{d}t} = \hat{\rho}_C M_1 - \gamma_C C_L, \tag{D.2e}$$

with $M_1 = P + P_m + P_p + C_I$ and $L = P + C_I + C_L$.

D.3 MM inhibition

$$\frac{\mathrm{d}P}{\mathrm{d}t} = \frac{\rho P}{1+\lambda L} + \frac{\hat{\rho}_S}{1+\mu M_2} - (\alpha+\gamma_P)P - \delta_m P P_m, \tag{D.3a}$$

$$\frac{\mathrm{d}P_m}{\mathrm{d}t} = \frac{\rho_m P_m}{1+\lambda_m L} + \frac{\hat{\rho}_{S_m}}{1+\mu_m M_2} - \gamma_{P_m} P_m, \tag{D.3b}$$

$$\frac{\mathrm{d}P_p}{\mathrm{d}t} = \frac{\rho_p P_p}{1+\lambda_p L} + \delta_m P P_m - \gamma_{P_p} P_p, \tag{D.3c}$$

$$\frac{\mathrm{dC}_I}{\mathrm{d}t} = \alpha P - \delta C_I C_L, \tag{D.3d}$$

$$\frac{\mathrm{dC}_L}{\mathrm{d}t} = \hat{\rho}_C M_2 - \gamma_C C_L, \tag{D.3e}$$

with $M_2 = P + P_m + P_p + C_I$ and $L = P + C_I + C_L$.

D.4 Existence, boundedness and positivity of solutions

Theorem D.1. *Considering the following set*

$$Q = \{(P, P_m, P_p, C_I, C_L) \in \mathbb{R}^5 : P, P_m, P_p, C_I, C_L > 0\}, \tag{D.4}$$

and the initial values in Q

$$\begin{aligned} P(t_0) = P^0, P_m(t_0) = P_m^0, P_p(t_0) = P_p^0, \\ C_I(t_0) = C_I^0, C_L(t_0) = C_L^0, \end{aligned} \tag{D.5}$$

then, the initial value problem for either equations (D.3) and (D.2) has a unique local-in-time solution for each $t \in [t_0 - \epsilon, t_0 + \epsilon]$, for some value $\epsilon > 0$.

Proof. Having same definitions in the proof of Theorem B.1, the existence of a solution for systems (D.3) and (D.2) is guaranteed for each $(P, P_m, P_p, C_I, C_L) \in Q$ by continuity of their right hand side functions. The fact that the partial derivatives of such functions are continuous and finite implies they are locally Lipschitz continuous. Therefore, by the Picard–Lindelöf theorem the solutions of systems (D.3) and (D.2) with initial values (D.5) are unique and local-in-time. □

Theorem D.2. *The solutions of equation (D.3) with $(P^0, P_m^0, P_p^0, C_I^0, C_L^0) \in Q$ are positive.*

Proof. Following the same procedure of Theorem B.2,

$$\frac{\mathrm{d}P}{\mathrm{d}t} > -(\alpha + \gamma_P + \delta_m P_m)P \implies P > P^0 \mathrm{e}^{-(\alpha+\gamma_P)t - \delta_m \int_{t_0}^{t} P_m \, \mathrm{d}t} > 0, \tag{D.6a}$$

$$\frac{\mathrm{d}P_m}{\mathrm{d}t} > -\gamma_{P_m} P \implies P_m > P_m^0 \mathrm{e}^{-\gamma_{P_m} t} > 0, \tag{D.6b}$$

$$\frac{\mathrm{d}P_p}{\mathrm{d}t} > -\gamma_{P_p} P \implies P_p > P_p^0 \mathrm{e}^{-\gamma_{P_p} t} > 0, \tag{D.6c}$$

$$\frac{\mathrm{dC}_I}{\mathrm{d}t} > -\delta C_I C_L \implies C_I > C_I^0 \mathrm{e}^{-\delta \int_{t_0}^{t} C_L \mathrm{d}t} > 0, \tag{D.6d}$$

$$\frac{\mathrm{dC}_L}{\mathrm{d}t} > -\gamma_C C_L \implies C_L > C_L^0 \mathrm{e}^{-\gamma_C t} > 0. \tag{D.6e}$$

□

Theorem D.3. *The solutions of equation (D.2) with $(P^0, P_m^0, P_p^0, C_I^0, C_L^0) \in Q$ are positive.*

Proof. Following the previous procedure, then

$$\frac{\mathrm{d}P}{\mathrm{d}t} > -\alpha P - \delta_m P P_m \implies P > P^0 \mathrm{e}^{-\alpha t - \delta_m \int_{t_0}^{t} P_m \, \mathrm{d}t} > 0, \tag{D.7a}$$

$$\frac{\mathrm{d}P_m}{\mathrm{d}t} > -\gamma_{P_m} P_m \implies P_m > P_m^0 \mathrm{e}^{-\gamma_{P_m} t} > 0, \tag{D.7b}$$

TABLE E.1. Results of the fitting of the proliferation and inhibition parameters of equations (E.1) and (E.2). $\lambda = 9.51/9.51 = 1$ and $\lambda_m = 9.51/36.61 = 0.26$ are here considered to find only $\hat{\theta}_1$.

		WT-MM		FD-MM	
		value	CI	value	CI
$\hat{\theta}_1$	ρ	0.47	0.25	0	0
	ρ_p	–	–	0.56	0.33
	γ_P	0.21	0.18	0.25	0.24
$\hat{\theta}_2$	ρ	4.77	104	0	0
	ρ_p	–	–	0.43	0.39
	λ	0.04	1.02	0	0
	λ_m	–	–	0.59	2.22
	γ_P	4.55	104.34	0.09	0.53

$$\frac{\mathrm{d}P_p}{\mathrm{d}t} > -\gamma_{P_p} P_p \implies P_p > P_p^0 \mathrm{e}^{-\gamma_{P_p} t} > 0, \tag{D.7c}$$

$$\frac{C_I}{\mathrm{d}t} > -\delta C_I C_L \implies C_I > C_I^0 \mathrm{e}^{-\delta \int_{t_0}^{t} C_L \mathrm{d}t} > 0, \tag{D.7d}$$

$$\frac{\mathrm{dC}_L}{\mathrm{d}t} > -\gamma_C C_L \implies C_L > C_L^0 \mathrm{e}^{-\delta t} > 0. \tag{D.7e}$$

□

Theorem D.4. *The solutions of equation (D.3) with* $(P^0, P_m^0, P_p^0, C_I^0, C_L^0) \in Q$ *are bounded.*

Proof. Following the same procedure in the proof of Theorem B.4, then P, P_m, P_p, C_I, C_L are bounded. □

Theorem D.5. *The solutions of equation (D.2) with* $(P^0, P_m^0, P_p^0, C_I^0, C_L^0) \in Q$ *are bounded.*

Proof. Following the same procedure in the proof of theorem B.5, then P, P_m, P_p, C_I, C_L are bounded. □

APPENDIX E. PROLIFERATION IN THE MM MODEL

Considering $\rho_m = \rho_p = \lambda_m = \lambda_p = \hat{\rho}_S = \hat{\rho}_{S_m} = \mu = \mu_m = \alpha = \delta_m = \gamma_{P_m} = \gamma_{P_p} = \delta = \hat{\rho}_C = \gamma_C = \mu_T = \delta_T = \gamma_T = P_m(0) = P_p(0) = C_I(0) = C_L(0) = T(0) = 0$ in equation (2.1). Thus, the model (Eq. A.4) becomes

$$\frac{\mathrm{d}P}{\mathrm{d}t} = \frac{\rho P}{1 + \lambda P} - \gamma_P P, \tag{E.1}$$

which describes the WT cell population growth. Analogously, by setting $\rho = \rho_p = \lambda = \lambda_p = \hat{\rho}_S = \hat{\rho}_{S_m} = \mu = \mu_m = \alpha = \delta_m = \gamma_{P_m} = \gamma_{P_p} = \delta = \hat{\rho}_C = \gamma_C = \mu_T = \delta_T = \gamma_T = P(0) = P_p(0) = C_I(0) = C_L(0) = T(0) = 0$, then,

$$\frac{\mathrm{d}P_m}{\mathrm{d}t} = \frac{\rho_m P_m}{1 + \lambda_m P_m} - \gamma_{P_m} P_m, \tag{E.2}$$

describes the mutant cell population growth alone. The sets of parameters considered to adjust these models are

$$\text{WT: } \theta_1 = \{\rho, \gamma_P\}, \theta_2 = \{\rho, \lambda, \gamma_P\}, \tag{E.3a}$$

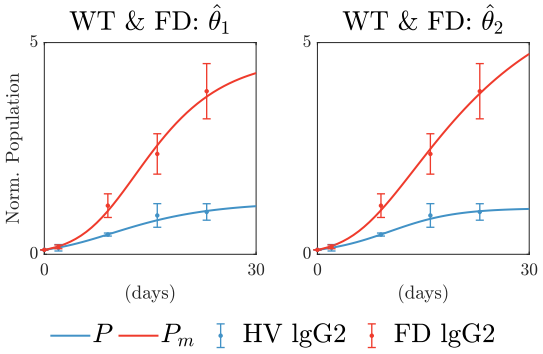

FIGURE E.1. MM proliferation curves for equations (E.1) and (E.2) with initial conditions $P(0) = 1/9.51$ and $P_m(0) = 1/9.51$, based on HV-IgG2 data from Table E.1. The data were normalized by dividing each value by the maximum value of 9.51.

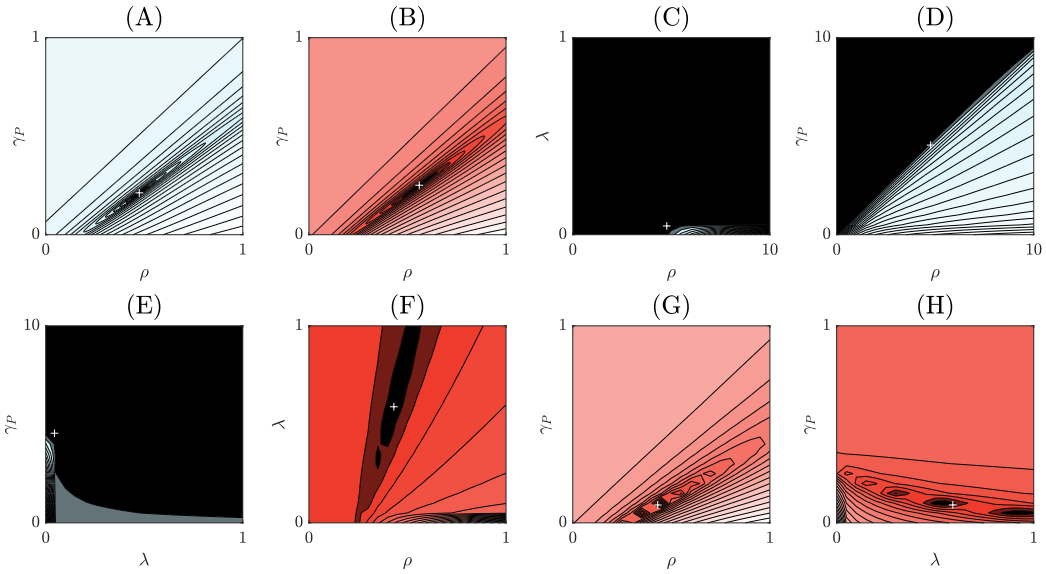

FIGURE E.2. Likelihood surface for $\hat{\theta}_2$ and equations (E.1)–(E.2). (A) WT: $\hat{\theta}_1$. (B) FD: $\hat{\theta}_1$. (C–E) WT: $\hat{\theta}_2$. (F–H) FD: $\hat{\theta}_2$. Despite the apparent good fitting of $\hat{\theta}_2$ shown in Figure E.1, it is practically non-indentifiable.

$$\text{FD: } \theta_1 = \{\rho_m, \gamma_{P_m}\}, \theta_2 = \{\rho_m, \lambda_m, \gamma_{P_m}\}. \tag{E.3b}$$

The fitting is shown in Table E.1 and represented in Figure E.1. The likelihood surface shown in Figure E.2 reveals that only $\hat{\theta}_1$ is identifiable. Thus, considering $H_0 : \rho_m - \rho = 0$, the two sample t-statistic is calculated with $t = (\hat{\rho} - \hat{\rho}_m)/(\text{CI}_\rho^2/5 + \text{CI}_{\rho_m}^2/5)^{1/2}$, resulting in $t = -0.486$, revealing that the difference between the ρ terms is not statistically significant with $t(\alpha = 0.05, df = 4)$ and p-value$= P(|t| \geq 0.4866) = 0.6524$, which is consistent with results attained in Section 3.1.

Appendix F. Phenotype-transferred model

F.1 LOG inhibition

The steady states for the model equation (3.4) are

$$P_1 = 0, P_{m1} = 0, P_{p1} = 0, \tag{F.1}$$

$$P_2 = 0, P_{m2} = 0, P_{p2} = \frac{1}{\lambda_p}, \tag{F.2}$$

$$P_3 = 0, P_{m3} = \frac{1}{\lambda_m}, P_{p3} = 0, \tag{F.3}$$

$$P_4 = 0, P_{m4} + P_{p4} = \frac{1}{\lambda_m}, \text{when } \frac{1}{\lambda_p} = \frac{1}{\lambda_m}, \tag{F.4}$$

$$P_5 = \frac{1}{\lambda}, P_{m5} = 0, P_{p5} = 0, \tag{F.5}$$

$$P_6 + P_{p6} = \frac{1}{\lambda}, P_{m6} = 0, \text{when } \frac{1}{\lambda_p} = \frac{1}{\lambda}, \tag{F.6}$$

$$P_7 = \frac{\rho_p(\lambda_m - \lambda_p)(\delta_m + \rho(\lambda - \lambda_m))}{\delta_m \lambda_m(\lambda\rho - \lambda_m(\rho - \rho_p) - \lambda_p\rho_p)}, \tag{F.7a}$$

$$P_{m7} = \frac{\rho(\lambda_m - \lambda)}{\delta_m \lambda_m}, \tag{F.7b}$$

$$P_{p7} = \frac{\rho(\lambda - \lambda_m)(\delta_m + \rho(\lambda - \lambda_m))}{\delta_m \lambda_m(\lambda\rho + \lambda_m(\rho_p - \rho) - \lambda_p\rho_p)}. \tag{F.7c}$$

(F.7d)

F.2 MM inhibition

Taking $\hat{\rho}_S = \hat{\rho}_{S_m} = \mu = \mu_m = \alpha = \delta = \hat{\rho}_C = \gamma_C = \delta_T = \gamma_T = C_I(0) = C_L(0) = T(0) = 0$, in model equation (A.4), then

$$\frac{\mathrm{d}P}{\mathrm{d}t} = \frac{\rho P}{1 + \lambda(P + P_m + P_p)} - \gamma_P P - \delta_m P P_m, \tag{F.8a}$$

$$\frac{\mathrm{d}P_m}{\mathrm{d}t} = \frac{\rho_m P_m}{1 + \lambda_m(P + P_m + P_p)} - \gamma_{P_m} P_m, \tag{F.8b}$$

$$\frac{\mathrm{d}P_p}{\mathrm{d}t} = \frac{\rho_p P_p}{1 + \lambda_p(P + P_m + P_p)} - \gamma_{P_p} P_p + \delta_m P P_m. \tag{F.8c}$$

Adopting the same approach used in Section 3.2, the numerical stability and bifurcation with $\delta_m \in [0, 50]$ and $P(0)/P_m(0) \in [0, 2]$ for model equation (F.8) is shown in Figure F.1 and the steady states are

$$P_1 = 0, P_{m1} = 0, P_{p1} = 0, \tag{F.9}$$

$$P_2 = 0, P_{m2} = 0, P_{p2} = \frac{\rho_p}{\gamma_{P_p}\lambda_p} - \frac{1}{\lambda_p}, \tag{F.10}$$

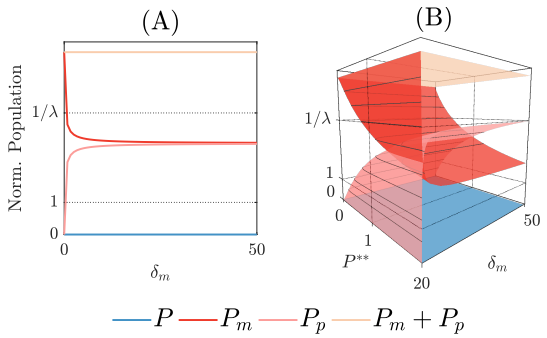

FIGURE F.1. Bifurcation maps for mutated-phenotype cells varying δ_m and $P(0)/P_m(0)$ in submodel (3.4) based on $\hat{\theta}_1$ from Table E.1. (A) Bifurcation map illustrating also P_m and P_p with $P(0) = P_m(0)$ and $P_p(0) = 0$. (B) A 3D representation of the stability of P_m and P_p varying δ_m and $P^{**} \equiv P(0)/P_m(0)$. Long-term cell competition is described in equation (F.12). These simulations support the analysis of Section 3.2.

$$P_3 = 0, P_{m3} = \frac{\rho_m}{\gamma_{P_m}\lambda_m} - \frac{1}{\lambda_m}, P_{p3} = 0, \tag{F.11}$$

$$P_4 = 0, P_{m4} + P_{p4} = \frac{\rho_m}{\gamma_{P_m}\lambda_m} - \frac{1}{\lambda_m}, \text{when } \frac{\rho_p}{\gamma_{P_p}\lambda_p} - \frac{1}{\lambda_p} = \frac{\rho_m}{\gamma_{P_m}\lambda_m} - \frac{1}{\lambda_m}, \tag{F.12}$$

$$P_5 = \frac{\rho}{\lambda\gamma_P} - \frac{1}{\lambda}, P_{m5} = 0, P_{p5} = 0, \tag{F.13}$$

$$P_6 + P_{p6} = \frac{\rho}{\lambda\gamma_P} - \frac{1}{\lambda}, P_{m6} = 0, \text{when } \frac{\rho_p}{\gamma_{P_p}\lambda_p} - \frac{1}{\lambda_p} = \frac{\rho}{\gamma_P\lambda} - \frac{1}{\lambda}, \tag{F.14}$$

$$P_7 = -\frac{((\lambda P_{m7}+1)(\delta_m P_{m7}+\gamma_P)-\rho)(\gamma_{P_p}(\lambda-\lambda_p)(\delta_m P_{m7}+\gamma_P)-\lambda\rho_p(\delta_m P_{m7}+\gamma_P)+\gamma_{P_p}\lambda_p\rho)}{\lambda(\delta_m P_{m7}+\gamma_P)((\delta_m P_{m7}+\gamma_{P_p})((\lambda-\lambda_p)(\delta_m P_{m7}+\gamma_P)+\lambda_p\rho)-\lambda\rho_p(\delta_m P_{m7}+\gamma_P))}, \tag{F.15a}$$

$$P_{m7} = \frac{\gamma_{P_{m7}}\lambda_m\rho}{\delta_m(\gamma_{P_{m7}}(\lambda_m-\lambda)+\lambda\rho_m)} - \frac{\gamma_P}{\delta_m}, \tag{F.15b}$$

$$P_{p7} = -\frac{\delta_m P_{m7}((\lambda P_{m7}+1)(\delta_m P_{m7}+\gamma_P)-\rho)((\lambda-\lambda_p)(\delta_m P_{m7}+\gamma_P)+\lambda_p\rho)}{\lambda(\delta_m P_{m7}+\gamma_P)((\delta_m P_{m7}+\gamma_{P_p})((\lambda-\lambda_p)(\delta_m P_{m7}+\gamma_P)+\lambda_p\rho)-\lambda\rho_p(\delta_m P_{m7}+\gamma_P))}, \tag{F.15c}$$

APPENDIX G. DIFFERENTIATION MODEL

G.1 LOG inhibition

The steady states for the model equation (3.5) are

$$P = 0, C_I = c. \tag{G.1}$$

The resulting stability condition derived from the eigenvalues of the Jacobian matrix is given by

$$C_I > \frac{\rho - \alpha}{\lambda\rho}. \tag{G.2}$$

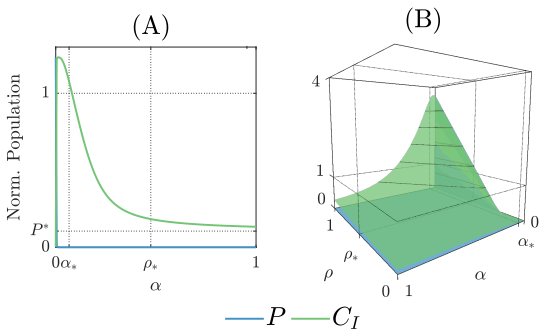

FIGURE G.1. Bifurcation maps of WT osteoprogenitor's differentiation in the MM model of equation (G.3). (A) Bifurcation in α with $\hat{\theta}_1$ from Table E.1. (B) Bifurcation in ρ and α. P^*: initial condition $P(0) = 1/9.51$. ρ_*: ρ in $\hat{\theta}_1$. α_*: 1/16. Note that carrying capacity is also limited by γ_P, which might imply populations larger than $1/\lambda$. The net population decreases substantially when α is close to ρ.

G.2 MM inhibition

Considering the WT tissue model of equation (C.3) without the osteoclastic lineage, then

$$\frac{\mathrm{d}P}{\mathrm{d}t} = \frac{\rho P}{1 + \lambda(P + C_I)} - (\alpha + \gamma_P)P, \tag{G.3a}$$

$$\frac{\mathrm{dC}_I}{\mathrm{d}t} = \alpha P. \tag{G.3b}$$

The steady states are

$$P = 0, C_I = c, \tag{G.4}$$

The stability condition derived as above is

$$C_I > \frac{\rho - (\alpha + \gamma_P)}{\lambda(\alpha + \gamma_P)}. \tag{G.5}$$

Figure G.1 shows the bifurcation analysis with $\rho \in [0, 1]$ and $\alpha \in [0, 1]$, illustrating how the steady state of C_I tends to $P(0)$ when the differentiation rate increases. These simulations support the conclusions of Section 3.3.

APPENDIX H. INHIBITED WT TISSUE MODEL W/O STEM CELLS

H.1 LOG inhibition

Considering $(1 - \lambda(P + C_I + C_L)) > 0$, the steady states for the model equation (3.7) are

$$P_1 = 0, C_{I1} = 0, C_{L1} = 0. \tag{H.1}$$

$$P_2 = \frac{\delta(\rho(1 - \lambda C_{L2}) - \alpha)C_{L2}}{\lambda\rho(\alpha + \delta C_{L2})}, \tag{H.2a}$$

$$C_{I2} = \frac{\alpha(\rho(1-\lambda C_{L2})-\alpha)}{\lambda\rho(\alpha+\delta C_{L2})}, \tag{H.2b}$$

$$C_{L2} = \frac{(\rho-\alpha)\hat{\rho}_C}{\lambda\rho(\gamma_C+\hat{\rho}_C)}. \tag{H.2c}$$

For studying the model stability, the Jacobian matrix (J) is defined and the characteristic polynomial p is calculated. The Routh–Hurtwitz criteria is used, verifying that all leading principal minors $\Delta_k(p)$ of the Hurtwitz matrix $H(p)$ are positive, such that,

$$\begin{aligned} J(P^*, C_I^*, C_L^*) &\implies \lambda_a x^3 + \lambda_b x^2 + \lambda_c x + \lambda_d = 0 \\ &\implies \Delta_3(p) = \left\{\lambda_b > 0, \lambda_b\lambda_c - \lambda_a\lambda_d > 0, \lambda_b\lambda_c\lambda_d - \lambda_a\lambda_d^2 > 0\right\}. \end{aligned} \tag{H.3}$$

Then, the stability conditions are

$$J = \begin{pmatrix} -\alpha - \lambda\rho(L+P) - \gamma_P + \rho & -\lambda\rho P & -\lambda\rho P \\ \alpha & -\delta C_L & -C_I\delta \\ \hat{\rho}_C & \hat{\rho}_C & -\gamma_C \end{pmatrix} \tag{H.4}$$

$$\lambda_a = 1, \tag{H.5a}$$

$$\lambda_b = \alpha + \rho(\lambda(L+P)-1) + \delta C_L + \gamma_C + \gamma_P, \tag{H.5b}$$

$$\begin{aligned} \lambda_c =& \alpha\delta C_L + \alpha\gamma_C + \alpha\lambda\rho P + \delta\lambda\rho C_L(L+P) + \gamma_C\lambda\rho(L+P) + \delta\hat{\rho}_C C_I \\ &+ \delta\gamma_C C_L + \delta\gamma_P C_L - \delta\rho C_L + \gamma_C\gamma_P - \gamma_C\rho + \lambda\rho\hat{\rho}_C P, \end{aligned} \tag{H.5c}$$

$$\begin{aligned} \lambda_d =& \alpha(\delta\hat{\rho}_C C_I + \delta\gamma_C C_L + \lambda\rho P(\gamma_C+\hat{\rho}_C)) + \delta\gamma_C C_L(\rho(\lambda(L+P)-1)+\gamma_P) \\ &+ \delta\hat{\rho}_C(\lambda\rho P(C_I+C_L) + C_I\rho(\lambda(C_I+C_L)-1) + \gamma_P C_I). \end{aligned} \tag{H.5d}$$

$$\begin{aligned} J(P_1, C_{I1}, C_{L1}) &\implies \lambda_a = 1, \lambda_b = \alpha + \gamma_C + \gamma_P - \rho, \lambda_c = \gamma_C(\alpha+\gamma_P-\rho), \lambda_d = 0. \\ &\implies \Delta_3(p) = \{\alpha + \gamma_C + \gamma_P - \rho > 0, \alpha^2\gamma_C + \alpha\gamma_C^2 + 2\alpha\gamma_C\gamma_P - 2\alpha\gamma_C\rho \\ &\quad + \gamma_C^2\gamma_P - \gamma_C^2\rho + \gamma_C\gamma_P^2 - 2\gamma_C\gamma_P\rho + \gamma_C\rho^2 > 0, \varnothing\} \end{aligned} \tag{H.6}$$

$$\begin{aligned} J(P_2, C_{I2}, C_{L2}) \implies& \lambda_a = 1, \lambda_b = \frac{\gamma_C(\alpha+\gamma_P-\rho)(\delta-\lambda\rho)}{\lambda\rho(\gamma_C+\hat{\rho}_C)} \\ &+ \frac{\alpha\gamma_C\lambda\rho(\alpha+\gamma_P-\rho)}{-\delta\hat{\rho}_C(\alpha+\gamma_P) + \rho\hat{\rho}_C(\alpha\lambda+\delta) + \alpha\gamma_C\lambda\rho} - \frac{\delta(\alpha+\gamma_P-\rho)}{\lambda\rho} + \gamma_C, \\ &\lambda_c = \frac{\gamma_C(\alpha+\gamma_P-\rho)(\delta-\lambda\rho)}{\lambda\rho(\gamma_C+\hat{\rho}_C)} + \frac{\alpha\gamma_C\lambda\rho(\alpha+\gamma_P-\rho)}{-\delta\hat{\rho}_C(\alpha+\gamma_P) + \rho\hat{\rho}_C(\alpha\lambda+\delta) + \alpha\gamma_C\lambda\rho} \\ &- \frac{\delta(\alpha+\gamma_P-\rho)}{\lambda\rho} + \gamma_C, \lambda_d = \frac{\delta\gamma_C\hat{\rho}_C(\alpha+\gamma_P-\rho)^2}{\lambda\rho(\gamma_C+\hat{\rho}_C)}. \\ \implies& \Delta_3(p) = \left\{\lambda_b > 0, \lambda_b\lambda_c - \lambda_a\lambda_d > 0, \lambda_b\lambda_c\lambda_d - \lambda_a\lambda_d^2 > 0\right\} \end{aligned} \tag{H.7}$$

H.2 MM inhibition

The WT tissue model of equation (C.2) without the stem cells flow is

$$\frac{\mathrm{d}P}{\mathrm{d}t} = \frac{\rho P}{1+\lambda(P+C_I+C_L)} - (\alpha+\gamma_P)P, \tag{H.8a}$$

$$\frac{\mathrm{dC}_I}{\mathrm{d}t} = \alpha P - \delta C_I C_L, \tag{H.8b}$$

$$\frac{\mathrm{dC}_L}{\mathrm{d}t} = \hat{\rho}_C(P + C_I) - \gamma_C C_L, \tag{H.8c}$$

and the steady states are

$$P_1 = 0, C_{I1} = 0, C_{L1} = 0. \tag{H.9}$$

$$P_2 = \frac{\delta(\rho - (\alpha+\gamma_P)(1+\lambda C_{L2}))\ C_{L2}}{\lambda(\alpha+\gamma_P)(\alpha+\delta C_{L2})}, \tag{H.10a}$$

$$C_{I2} = \frac{\alpha(\rho - (\alpha+\gamma_P)(1+\lambda C_{L2}))}{\lambda(\alpha+\gamma_P)(\alpha+\delta C_{L2})}, \tag{H.10b}$$

$$C_{L2} = \frac{\hat{\rho}_C(\rho - (\alpha+\gamma_P))}{\lambda(\alpha+\gamma_P)(\gamma_C+\hat{\rho}_C)}. \tag{H.10c}$$

Following the same procedure of the previous section, the stability conditions are

$$J = \begin{pmatrix} \dfrac{\rho(1+\lambda(C_I+C_L))}{(1+\lambda L)^2} - (\alpha+\gamma_P) & -\dfrac{\lambda\rho P}{(1+\lambda L)^2} & -\dfrac{\lambda\rho P}{(1+\lambda L)^2} \\ \alpha & -\delta C_L & -\delta C_I \\ \hat{\rho}_C & \hat{\rho}_C & -\gamma_C \end{pmatrix} \tag{H.11}$$

$$\lambda_a = 1, \tag{H.12a}$$

$$\lambda_b = \alpha - \frac{\rho(1+\lambda(C_I+C_L))}{(1+\lambda L)^2} + \delta C_L + \gamma_C + \gamma_P, \tag{H.12b}$$

$$\begin{aligned}\lambda_c = {} & \frac{\alpha\lambda\rho P}{(1+\lambda L)^2} + \alpha\delta C_L + \alpha\gamma_C - \frac{\delta\rho C_L(1+\lambda(C_I+C_L))}{(1+\lambda L)^2} - \frac{\gamma_C\rho(1+\lambda(C_I+C_L))}{(1+\lambda L)^2} \\ & + \frac{\lambda\rho\hat{\rho}_C P}{(1+\lambda L)^2} + \delta\hat{\rho}_C C_I + \delta\gamma_C C_L + \delta\gamma_P C_L + \gamma_C\gamma_P,\end{aligned} \tag{H.12c}$$

$$\begin{aligned}\lambda_d = {} & \frac{\alpha\gamma_C\left(\delta C_L(1+\lambda L)^2 + \lambda\rho P\right) + \alpha\hat{\rho}_C\left(\delta C_I(1+\lambda L)^2 + \lambda\rho P\right)}{(1+\lambda L)^2} \\ & + \frac{\delta\gamma_C C_L\left(\gamma_P(1+\lambda L)^2 - \rho(1+\lambda(C_I+C_L))\right)}{(1+\lambda L)^2} \\ & + \frac{\delta\hat{\rho}_C\left(C_I\gamma_P(1+\lambda L)^2 - \rho(\lambda P(C_I-C_L) + C_I\lambda(C_I+C_L) + C_I)\right)}{(1+\lambda L)^2}.\end{aligned} \tag{H.12d}$$

$$\begin{aligned} J(P_1, C_{I1}, C_{L1}) \implies & \lambda_a = 1, \lambda_b = \alpha + \gamma_C + \gamma_P - \rho, \lambda_c = \gamma_C(\alpha + \gamma_P - \rho), \lambda_d = 0. \\ \implies & \Delta_3(p) = \{\alpha + \gamma_C + \gamma_P - \rho > 0, \alpha^2\gamma_C + \alpha\gamma_C^2 + 2\alpha\gamma_C\gamma_P \\ & -2\alpha\gamma_C\rho + \gamma_C^2\gamma_P - \gamma_C^2\rho + \gamma_C\gamma_P^2 - 2\gamma_C\gamma_P\rho + \gamma_C\rho^2 > 0, \varnothing\}. \end{aligned} \tag{H.13}$$

$$\begin{aligned} J(P_2, C_{I2}, C_{L2}) \implies \lambda_a = 1, \lambda_b = {} & \frac{\alpha\gamma_C\lambda^2(\alpha+\gamma_P)^3(\alpha+\gamma_P-\rho)}{\lambda(\alpha+\gamma_P)(\rho\hat{\rho}_C((\alpha+\gamma_P)(\alpha\lambda-\delta)+\delta\rho) + \alpha\gamma_C\lambda\rho(\alpha+\gamma_P))} \\ & - \frac{\gamma_C(\alpha+\gamma_P-\rho)\left(\lambda(\alpha+\gamma_P)^2 - \delta\rho\right)}{\lambda(\alpha+\gamma_P)(\rho(\gamma_C+\hat{\rho}_C))} - \frac{\alpha\delta + \alpha\gamma_C\lambda - \delta\gamma_P + \delta\rho + \gamma_C\gamma_P\lambda}{\lambda(\alpha+\gamma_P)}, \end{aligned}$$

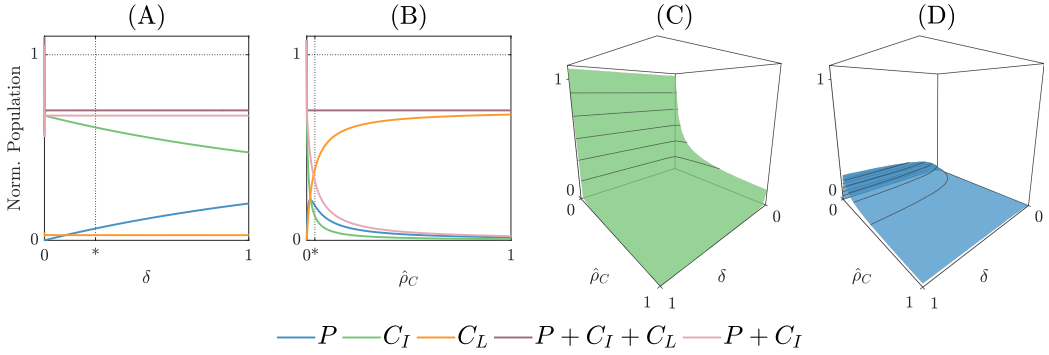

FIGURE H.1. Osteoclastogenesis bifurcation for osteoclasts of equation (H.8) varying δ and $\hat{\rho}_C$, with $\hat{\theta}_1$ from Table E.1 and $\alpha = 1/16$, $\gamma_C = 1/30$. (A) Bifurcation varying δ_m. (B) Bifurcation varying $\hat{\rho}_C$. (C) Osteocyte's bifurcation surface. (D) Osteoprogenitor's bifurcation surface. *: $\delta = 1/4$, $\hat{\rho}_C = 0.0014$. Variations in $\hat{\rho}_C$ reveal a stronger influence over bone matrix than variations in δ.

$$
\begin{aligned}
&\lambda_c = (\delta\gamma_C\hat{\rho}_C(\alpha+\gamma_P-\rho)(\hat{\rho}_C(-\rho(\alpha+\gamma_P)(\lambda\left(\alpha^2+\alpha(6\gamma_C+\gamma_P)+2\gamma_C\gamma_P\right)\\
&-\delta(2\alpha+\gamma_C+2\gamma_P))+(\alpha+\gamma_P)^3(\lambda(\alpha+2\gamma_C)-\delta)-\delta\rho^2(\alpha+\gamma_C+\gamma_P))\\
&+\hat{\rho}_C^2\left(-\rho(\alpha+\gamma_P)(\lambda(3\alpha+\gamma_P)-\delta)+\lambda(\alpha+\gamma_P)^3-\delta\rho^2\right)\\
&+\gamma_C\lambda(\alpha+\gamma_P)\left((\alpha+\gamma_C)(\alpha+\gamma_P)^2-\rho(\gamma_P(\alpha+\gamma_C)+\alpha(\alpha+3\gamma_C))\right)))/\\
&(\lambda\rho(\alpha+\gamma_P)(\gamma_C+\hat{\rho}_C)^2(\hat{\rho}_C(\alpha+\gamma_P)(\alpha\lambda-\delta)+\alpha\gamma_C\lambda(\alpha+\gamma_P)+\delta\rho\hat{\rho}_C)),\\
&\lambda_d = \frac{\delta\gamma_C\hat{\rho}_C(\alpha+\gamma_P-\rho)^2}{\lambda\rho(\gamma_C+\hat{\rho}_C)}.\\
\implies\ &\Delta_3(p) = \left\{\lambda_b>0, \lambda_b\lambda_c-\lambda_a\lambda_d>0, \lambda_b\lambda_c\lambda_d-\lambda_a\lambda_d^2>0\right\}.
\end{aligned}
\tag{H.14}
$$

Additionally, the bifurcation maps varying $\hat{\rho}_C$ and δ are shown in Figure H.1, revealing also the inverse relation between active osteoclasts and osteocytes.

APPENDIX I. INHIBITED DYSPLASTIC TISSUE MODEL W/O STEM CELLS

I.1 LOG inhibition

Considering $(1-\lambda(P+P_m+C_I+C_L))>0$ and $(1-\lambda_m(P+P_m+C_I+C_L))>0$, the steady states for the model of equation (3.8) are

$$P_1 = 0, P_{m1} = 0, C_{I1} = 0, C_{L1} = 0. \tag{I.1}$$

$$P_2 = 0, P_{m2} = \frac{\gamma_C}{\lambda_m(\gamma_C+\hat{\rho}_C)}, C_{I2} = 0, C_{L2} = \frac{\hat{\rho}_C}{\lambda_m(\gamma_C+\hat{\rho}_C)}. \tag{I.2}$$

$$P_3 = \frac{\delta(\rho(1-\lambda C_{L3})-\alpha)C_{L3}}{(\alpha+\delta C_{L3})\lambda\rho}, \tag{I.3a}$$

$$P_{m3} = 0, \tag{I.3b}$$

$$C_{I3} = \frac{\alpha(\rho(1-\lambda C_{L3})-\alpha)}{\lambda\rho(\alpha+\delta C_{L3})}, \tag{I.3c}$$

$$C_{L3} = \frac{(\rho-\alpha)\hat{\rho}_C}{\lambda\rho(\gamma_C+\hat{\rho}_C)}. \tag{I.3d}$$

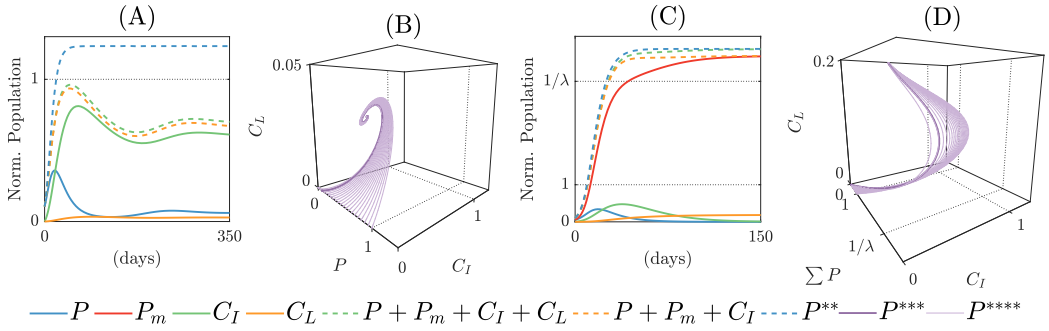

FIGURE I.1. Phase maps for the WT tissue of equation (H.8) and the FD tissue of equation (I.5) without stem cells, with $\hat{\theta}_1$ from Table E.1 and $\alpha = 1/16$, $\delta = 1/4$, $\hat{\rho}_C = 0.0014$, $\gamma_C = 1/30$. (A) Simulation for WT tissue. (B) WT orbits. (C) Simulation for FD tissue. (D) FD orbits. P^{**} is the simulation curve of P from Figure E.1. P^{***}: initial conditions $P(0) = P_m(0) = 1/9.51$ used in (A) and (C), respectively. P^{****}: additional simulations with initial conditions $P(0) = P_m(0) = [0, 1]$. In presence of mutant cells, the system stability changes from a spiral sink to an asymptotic sink.

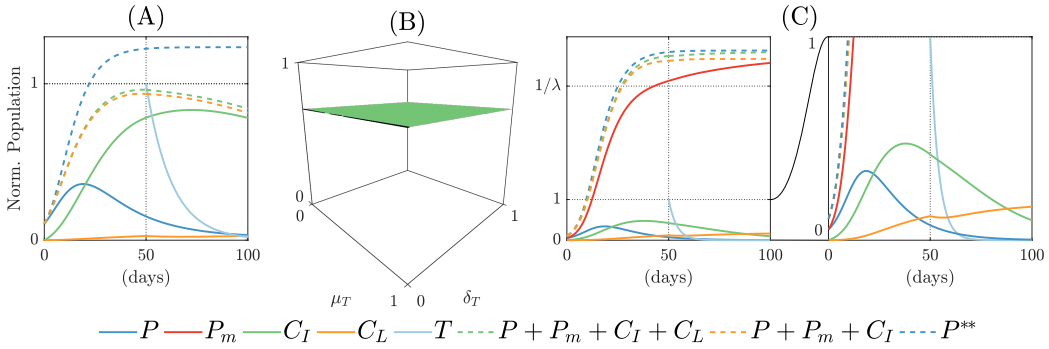

FIGURE I.2. Denosumab intervention in $T(t = 50) = 1$ considering the MM model (Eq. A.4), $\hat{\theta}_1$ from Table E.1 and $\alpha = 1/16$, $\delta = 1/4$, $\hat{\rho}_C = 0.0014$, $\gamma_C = 1/30$. (A) WT treated tissue. (B) Treated osteocyte's bifurcation varying δ_T and μ_T. (C) FD treated tissue. P^{**} is the simulation curve of P from Figure 3. Steady states do not change after treatment, revealing just transitory effects.

$$P_4 = \frac{\delta\hat{\rho_C}(\alpha-\rho)(\gamma_C(\alpha+\rho(\lambda P_{m4}-1))+\lambda\rho\hat{\rho_C}P_{m4})}{\lambda\rho(\gamma_C+\hat{\rho_C})(-\alpha\delta\hat{\rho_C}+\alpha\lambda\rho(\gamma_C+\hat{\rho_C})+\delta\rho\hat{\rho_C})}, \tag{I.4a}$$

$$C_{I4} = -\frac{\alpha(\gamma_C(\alpha+\rho(\lambda P_{m4}-1))+\lambda\rho\hat{\rho_C}P_{m4})}{-\alpha\delta\hat{\rho_C}+\alpha\lambda\rho(\gamma_C+\hat{\rho_C})+\delta\rho\hat{\rho_C}}, \tag{I.4b}$$

$$C_{L4} = \frac{\hat{\rho_C}(\rho-\alpha)}{\lambda\rho(\gamma_C+\hat{\rho_C})}, \text{when } \frac{1-\alpha/\rho}{\lambda} = \frac{1}{\lambda_m}. \tag{I.4c}$$

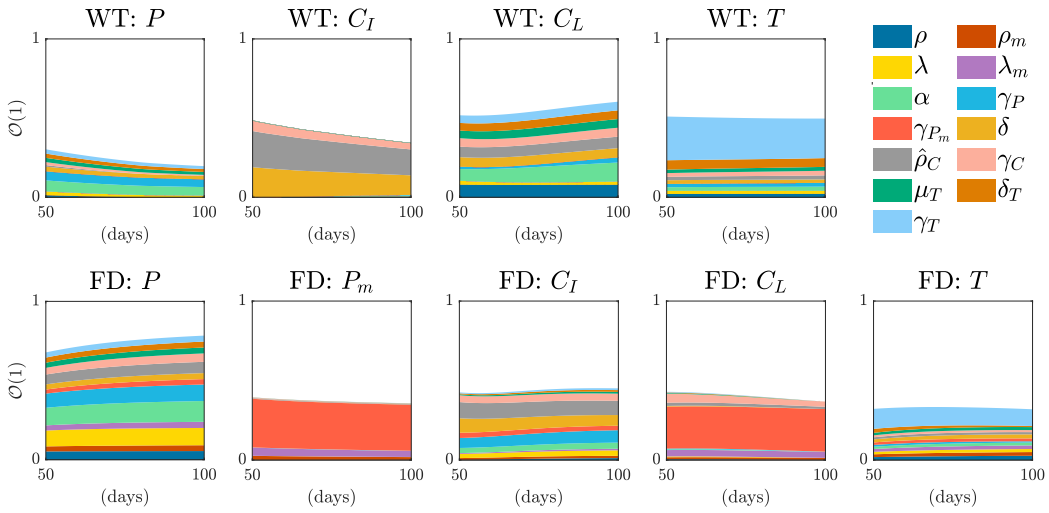

FIGURE I.3. Stacked area chart with the variance sensitivity analysis for WT and dysplastic tissues after denosumab intervention in time $t = 50$ for the MM model (Eq. A.4). $P(0) = P_m(0) = 1/9.51$, $P_p(0) = C_I(0) = C_L(0) = T(0) = 0$ and $T(50) = 1$. First order Jansen–Sobol's indices [38] with $N \sim (1/2, 1/4)$ for all parameters and 1.5×10^6 iterations for $t = [50, 100]$. No relevant influence is found for μ_T, δ_T or γ_T. Nevertheless, γ_{P_m} does reveal a strong influence in osteoclasts.

I.2 MM inhibition

Considering the model of equation (A.4) with $\rho_p = \lambda_p = \hat{\rho}_S = \hat{\rho}_{S_m} = \mu = \mu_m = \delta_m = \gamma_{P_p} = \mu_T = \delta_T = \gamma_T = P_p(0) = T(0) = 0$, results in

$$\frac{\mathrm{d}P}{\mathrm{d}t} = \frac{\rho P}{1 + \lambda(P + P_m + C_I + C_L)} - (\alpha + \gamma_P)P, \tag{I.5a}$$

$$\frac{\mathrm{d}P_m}{\mathrm{d}t} = \frac{\rho_m P_m}{1 + \lambda_m(P + P_m + C_I + C_L)} - \gamma_{P_m} P_m, \tag{I.5b}$$

$$\frac{\mathrm{dC}_I}{\mathrm{d}t} = \alpha P - \delta C_I C_L, \tag{I.5c}$$

$$\frac{\mathrm{dC}_L}{\mathrm{d}t} = \hat{\rho}_C(P + P_m + C_I) - \gamma_C C_L. \tag{I.5d}$$

The steady states are

$$P_1 = 0, P_{m1} = 0, C_{I1} = 0, C_{L1} = 0. \tag{I.6}$$

$$P_2 = 0, P_{m2} = \frac{\gamma_C(\rho_m - \gamma_{P_m})}{\gamma_{P_m}\lambda_m(\gamma_C + \hat{\rho}_C)}, C_{I2} = 0, C_{L2} = \frac{\hat{\rho}_C(\rho_m - \gamma_{P_m})}{\gamma_{P_m}\lambda_m(\gamma_C + \hat{\rho}_C)}. \tag{I.7}$$

$$P_3 = \frac{\delta\gamma_C\hat{\rho}_C(\alpha + \gamma_P - \rho)^2}{\lambda(\alpha + \gamma_P)(\gamma_C + \hat{\rho}_C)(\hat{\rho}_C(\alpha + \gamma_P)(\alpha\lambda - \delta) + \alpha\gamma_C\lambda(\alpha + \gamma_P) + \delta\rho\hat{\rho}_C)}, \tag{I.8a}$$

$$P_{m3} = 0, \tag{I.8b}$$

$$C_{I3} = \frac{\alpha\gamma_C(\alpha+\gamma_P-\rho)}{\hat{\rho}_C(\alpha+\gamma_P)(\alpha\lambda-\delta)+\alpha\gamma_C\lambda(\alpha+\gamma_P)+\delta\rho\hat{\rho}_C}, \tag{I.8c}$$

$$C_{L3} = -\frac{\hat{\rho}_C(\alpha+\gamma_P-\rho)}{\lambda(\alpha+\gamma_P)(\gamma_C+\hat{\rho}_C)}. \tag{I.8d}$$

$$P_4 = \frac{\delta\hat{\rho_C}(\alpha+\gamma_P-\rho)(\gamma_C(\alpha+\gamma_P)(\lambda P_{m4}+1)+\lambda\hat{\rho_C}(\alpha+\gamma_P)P_{m4}-\gamma_C\rho)}{\lambda(\alpha+\gamma_P)(\gamma_C+\hat{\rho_C})(\hat{\rho_C}(\alpha+\gamma_P)(\alpha\lambda-\delta)+\alpha\gamma_C\lambda(\alpha+\gamma_P)+\delta\rho\hat{\rho_C})}, \tag{I.9a}$$

$$C_{I4} = \frac{\alpha\gamma_C(\rho-(\alpha+\gamma_P)(\lambda P_{m4}+1))-\alpha\lambda\hat{\rho_C}(\alpha+\gamma_P)P_{m4}}{\hat{\rho_C}(\alpha+\gamma_P)(\alpha\lambda-\delta)+\alpha\gamma_C\lambda(\alpha+\gamma_P)+\delta\rho\hat{\rho_C}}, \tag{I.9b}$$

$$C_{L4} = -\frac{\hat{\rho_C}(\alpha+\gamma_P-\rho)}{\lambda(\alpha+\gamma_P)(\gamma_C+\hat{\rho_C})}, \text{when } \frac{\rho/(\alpha+\gamma_P)-1}{\lambda} = \frac{\rho_m-\gamma_{P_m}}{\gamma_{P_m}\lambda_m}. \tag{I.9c}$$

To support the conclusions attained in Section 3.5, Figure I.1 shows the additional simulations with the MM model of equations (H.8) and (I.5), revealing also the stability deviation from an spiral sink in the WT tissue to an asymptotic sink state in the FD tissue.

Appendix J. Denosumab and sensitivity analysis in the MM model

J.1 Treatment in LOG inhibited WT tissue

Considering the model of equation (3.7) with the treatment comportment T, such that $1-\mu_T T>0$, then

$$\frac{\mathrm{d}P}{\mathrm{d}t} = \rho P(1-\lambda(P+C_I+C_L))-\alpha P, \tag{J.1a}$$

$$\frac{\mathrm{dC}_I}{\mathrm{d}t} = \alpha P-\delta C_I C_L, \tag{J.1b}$$

$$\frac{\mathrm{dC}_L}{\mathrm{d}t} = \hat{\rho}_C(P+C_I)(1-\mu_T T)-\gamma_C C_L, \tag{J.1c}$$

$$\frac{\mathrm{d}T}{\mathrm{d}t} = -\delta_T T(P+C_I+C_L)-\gamma_T T. \tag{J.1d}$$

The steady states are

$$P_1 = 0, C_{I1} = 0, C_{L1} = 0. \tag{J.2}$$

$$P_2 = \frac{\delta(\rho(1-\lambda C_{L2})-\alpha)C_{L2}}{\lambda\rho(\alpha+\delta C_{L2})}, \tag{J.3a}$$

$$C_{I2} = \frac{\alpha(\rho(1-\lambda C_{L2})-\alpha)}{\lambda\rho(\alpha+\delta C_{L2})}, \tag{J.3b}$$

$$C_{L2} = \frac{(\rho-\alpha)\hat{\rho}_C}{\lambda\rho(\gamma_C+\hat{\rho}_C)}. \tag{J.3c}$$

J.2 Treatment in LOG inhibited FD tissue

Considering the model of equation (3.8) with the treatment comportment T, such that $1-\mu_T T>0$, then

$$\frac{\mathrm{d}P}{\mathrm{d}t} = \rho P(1-\lambda(P+P_m+C_I+C_L))-\alpha P, \tag{J.4a}$$

$$\frac{\mathrm{d}P_m}{\mathrm{d}t} = \rho_m P_m(1 - \lambda_m(P + P_m + C_I + C_L)), \tag{J.4b}$$
$$\frac{\mathrm{dC}_I}{\mathrm{d}t} = \alpha P - \delta C_I C_L, \tag{J.4c}$$
$$\frac{\mathrm{dC}_L}{\mathrm{d}t} = \hat{\rho}_C(P + P_m + C_I)(1 - \mu_T T) - \gamma_C C_L, \tag{J.4d}$$
$$\frac{\mathrm{d}T}{\mathrm{d}t} = -\delta_T T(P + C_I + C_L) - \gamma_T T. \tag{J.4e}$$

The steady states are

$$P_1 = 0, C_{I1} = 0, C_{L1} = 0. \tag{J.5}$$

$$P_2 = \frac{\delta(\rho - (\alpha + \gamma_P)(1 + \lambda C_{L2}))\ C_{L2}}{\lambda(\alpha + \gamma_P)(\alpha + \delta C_{L2})}, \tag{J.6a}$$
$$C_{I2} = \frac{\alpha(\rho - (\alpha + \gamma_P)(1 + \lambda C_{L2}))}{\lambda(\alpha + \gamma_P)(\alpha + \delta C_{L2})}, \tag{J.6b}$$
$$C_{L2} = \frac{\hat{\rho}_C(\rho - (\alpha + \gamma_P))}{\lambda(\alpha + \gamma_P)(\gamma_C + \hat{\rho}_C)}. \tag{J.6c}$$

J.3 Treatment in MM inhibited WT tissue

Considering the model of equation (H.8) with the treatment comportment T, then

$$\frac{\mathrm{d}P}{\mathrm{d}t} = \frac{\rho P}{1 + \lambda(P + C_I + C_L)} - (\alpha + \gamma_P)P, \tag{J.7a}$$
$$\frac{\mathrm{dC}_I}{\mathrm{d}t} = \alpha P - \delta C_I C_L, \tag{J.7b}$$
$$\frac{\mathrm{dC}_L}{\mathrm{d}t} = \hat{\rho}_C \frac{P + C_I}{1 + \mu_T T} - \gamma_C C_L, \tag{J.7c}$$
$$\frac{\mathrm{d}T}{\mathrm{d}t} = -\delta_T T(P + C_I + C_L) - \gamma_T T. \tag{J.7d}$$

The steady states are

$$P_1 = 0, P_{m1} = 0, C_{I1} = 0, C_{L1} = 0. \tag{J.8}$$

$$P_2 = 0, P_{m2} = \frac{\gamma_C}{\lambda_m(\gamma_C + \hat{\rho}_C)}, C_{I2} = 0, C_{L2} = \frac{\hat{\rho}_C}{\lambda_m(\gamma_C + \hat{\rho}_C)}. \tag{J.9}$$

$$P_3 = \frac{\delta(\rho(1 - \lambda C_{L3}) - \alpha)C_{L3}}{(\alpha + \delta C_{L3})\lambda\rho}, \tag{J.10a}$$
$$P_{m3} = 0, \tag{J.10b}$$
$$C_{I3} = \frac{\alpha(\rho(1 - \lambda C_{L3}) - \alpha)}{\lambda\rho(\alpha + \delta C_{L3})}, \tag{J.10c}$$

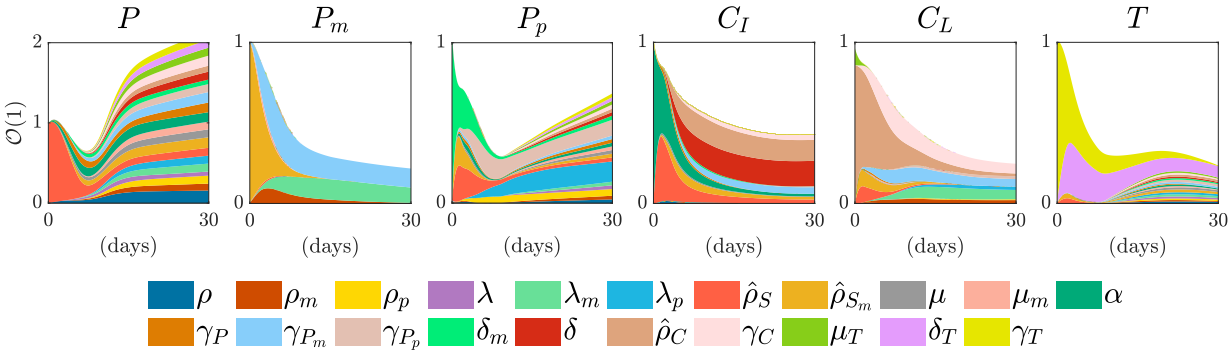

FIGURE J.1. Stacked area chart with the variance-based sensitivity analysis for the MM model with all parameters included for the first 30 days. $P(0) = P_m(0) = 1/9.51$, $P_p(0) = C_I(0) = C_L(0) = 0$ and $T(0) = 1$. The MM model of equation (A.4) shows similar weight to the LOG model of equation (2.1), although, the latter looks stronger in the dysplastic tissue, MM compensates it with the γ_i decay effect. Since the cell culture plate is almost empty in $t = 0$, the stem's flow, osteoclast activation and denosumab degradation are stronger in the first days. The mutant stem cells also have an indirect effect in the WT osteoprogenitors.

$$C_{L3} = \frac{(\rho - \alpha)\hat{\rho}_C}{\lambda\rho(\gamma_C + \hat{\rho}_C)}. \tag{J.10d}$$

$$P_4 = \frac{\delta\hat{\rho_C}(\alpha - \rho)(\gamma_C(\alpha + \rho(\lambda P_{m4} - 1)) + \lambda\rho\hat{\rho_C}P_{m4})}{\lambda\rho(\gamma_C + \hat{\rho_C})(-\alpha\delta\hat{\rho_C} + \alpha\lambda\rho(\gamma_C + \hat{\rho_C}) + \delta\rho\hat{\rho_C})}, \tag{J.11a}$$

$$C_{I4} = -\frac{\alpha(\gamma_C(\alpha + \rho(\lambda P_{m4} - 1)) + \lambda\rho\hat{\rho_C}P_{m4})}{-\alpha\delta\hat{\rho_C} + \alpha\lambda\rho(\gamma_C + \hat{\rho_C}) + \delta\rho\hat{\rho_C}}, \tag{J.11b}$$

$$C_{L4} = \frac{\hat{\rho_C}(\rho - \alpha)}{\lambda\rho(\gamma_C + \hat{\rho_C})}, \text{when } \frac{1 - \alpha/\rho}{\lambda} = \frac{1}{\lambda_m}. \tag{J.11c}$$

J.4 Treatment in MM inhibited FD tissue

Considering the model of equation (I.5) with the treatment comportment T, then

$$\frac{\mathrm{d}P}{\mathrm{d}t} = \frac{\rho P}{1 + \lambda(P + P_m + C_I + C_L)} - (\alpha + \gamma_P)P, \tag{J.12a}$$

$$\frac{\mathrm{d}P_m}{\mathrm{d}t} = \frac{\rho_m P_m}{1 + \lambda_m(P + P_m + C_I + C_L)} - \gamma_{P_m}P_m, \tag{J.12b}$$

$$\frac{\mathrm{dC}_I}{\mathrm{d}t} = \alpha P - \delta C_I C_L, \tag{J.12c}$$

$$\frac{\mathrm{dC}_L}{\mathrm{d}t} = \hat{\rho}_C\frac{P + P_m + C_I}{1 + \mu_T T} - \gamma_C C_L, \tag{J.12d}$$

$$\frac{\mathrm{d}T}{\mathrm{d}t} = -\delta_T T(P + C_I + C_L) - \gamma_T \tag{J.12e}$$

The steady states are

$$P_1 = 0, P_{m1} = 0, C_{I1} = 0, C_{L1} = 0. \tag{J.13}$$

$$P_2 = 0, P_{m2} = \frac{\gamma_C(\rho_m - \gamma_{P_m})}{\gamma_{P_m}\lambda_m(\gamma_C + \hat{\rho}_C)}, C_{I2} = 0, C_{L2} = \frac{\hat{\rho}_C(\rho_m - \gamma_{P_m})}{\gamma_{P_m}\lambda_m(\gamma_C + \hat{\rho}_C)}. \tag{J.14}$$

$$P_3 = \frac{\delta\gamma_C\hat{\rho}_C(\alpha + \gamma_P - \rho)^2}{\lambda(\alpha + \gamma_P)(\gamma_C + \hat{\rho}_C)(\hat{\rho}_C(\alpha + \gamma_P)(\alpha\lambda - \delta) + \alpha\gamma_C\lambda(\alpha + \gamma_P) + \delta\rho\hat{\rho}_C)}, \tag{J.15a}$$

$$P_{m3} = 0, \tag{J.15b}$$

$$C_{I3} = \frac{\alpha\gamma_C(\alpha + \gamma_P - \rho)}{\hat{\rho}_C(\alpha + \gamma_P)(\alpha\lambda - \delta) + \alpha\gamma_C\lambda(\alpha + \gamma_P) + \delta\rho\hat{\rho}_C}, \tag{J.15c}$$

$$C_{L3} = -\frac{\hat{\rho}_C(\alpha + \gamma_P - \rho)}{\lambda(\alpha + \gamma_P)(\gamma_C + \hat{\rho}_C)}. \tag{J.15d}$$

$$P_4 = \frac{\delta\hat{\rho_C}(\alpha + \gamma_P - \rho)(\gamma_C(\alpha + \gamma_P)(\lambda P_{m4} + 1) + \lambda\hat{\rho_C}(\alpha + \gamma_P)P_{m4} - \gamma_C\rho)}{\lambda(\alpha + \gamma_P)(\gamma_C + \hat{\rho_C})(\hat{\rho_C}(\alpha + \gamma_P)(\alpha\lambda - \delta) + \alpha\gamma_C\lambda(\alpha + \gamma_P) + \delta\rho\hat{\rho_C})}, \tag{J.16a}$$

$$C_{I4} = \frac{\alpha\gamma_C(\rho - (\alpha + \gamma_P)(\lambda P_{m4} + 1)) - \alpha\lambda\hat{\rho_C}(\alpha + \gamma_P)P_{m4}}{\hat{\rho_C}(\alpha + \gamma_P)(\alpha\lambda - \delta) + \alpha\gamma_C\lambda(\alpha + \gamma_P) + \delta\rho\hat{\rho_C}}, \tag{J.16b}$$

$$C_{L4} = -\frac{\hat{\rho_C}(\alpha + \gamma_P - \rho)}{\lambda(\alpha + \gamma_P)(\gamma_C + \hat{\rho_C})}, \text{when } \frac{\rho/(\alpha + \gamma_P) - 1}{\lambda} = \frac{\rho_m - \gamma_{P_m}}{\gamma_{P_m}\lambda_m}. \tag{J.16c}$$

J.5 Analysis of the MM models

Adopting the same procedure used in Section 3.6 for the MM models of equation (J.7) and (J.12), then no changes in system stability were observed after the treatment intervention, as it is shown in Figure I.2. The sensitivity analysis shown in Figure I.3 also reveals no relevant effect of μ_T, δ_T or γ_T.

Finally, considering the boundaries specified in Section 3.7, the first order Jansen–Sobol's indices are also computed for the MM model (Eq. A.4) with $N \sim (1/2, 1/4)$ for all parameters and 1.5×10^6 iterations for the first 30 days and the results are shown in Figure J.1.